The Reverse Approach for Monopile Scour

Hartvig, Peres Akrawi

Published in:
Coastal Engineering Journal

Publication date:
2012

Document Version
Early version, also known as pre-print

The Reverse Approach for Monopile Scour

Peres Akrawi Hartvig

Department of Civil Engineering, Aalborg University, Niels Bohrs Vej 8, 6700 Esbjerg, Denmark

Abstract

The present paper deals with the theoretical and numerical modeling of scouring and backfilling around an offshore monopile. Based on existing relations for the bed load and the bed update, and a new model for the sediment pickup, it demonstrates the possibility of computing the mean bed shear stress if the bed and bed update is estimated. The present concepts may be useful for developing methods for scour forecasting.

Keywords: Inverse, scouring, backfilling, scoured bed, monopile, sediment, Exner equation, bed load, suspended load, entrainment, pick-up, bed shear stress

1. Introduction

A common approach for simulating sediment transport deals with the phenomenon as a coupled series of casual events involving the *bed surface*, the *fluid flow* and the *sediment transport*. In such a perception, the bed surface influences the fluid flow which influences the sediment transport which influences the bed surface and so it continues. This is illustrated in the interaction triangle in Fig. 8.1 together with the links between each item, namely the transport equations for the fluid mass, fluid momentum and other relevant quantities, models for the bed load and suspended load and the Exner equation. This approach is adopted in e.g. Brørs (1999) or Roulund et al. (2005) and appears to represent the state-of-the-art within the field despite its inherent simplifications.

[Fig. 8.1 about here]

In the present study, I propose to use the components of this approach

as usual, although not quite as usual, since I will proceed counter-clockwise in Fig. 8.1 for the bed domain of interest. I begin by prescribing the bed elevation and the bed elevation rate. Then, I compute the corresponding sediment transport and fluid flow. This is why I have named the present approach as the *reverse* approach in contrast to the conventional approach that I will refer to as the *forward* approach. After drafting the reverse approach, I have discovered that it can be interpreted as a conventional *inverse method* defined by its aim to determine unknown *causes* based on observation of their *effects*.

In the present paper, I apply the reverse approach to the case of scour around a circular offshore monopile. To be precise, I consider the two special cases *scouring* and *backfilling* of the scour phenomenon, i.e. when the scour hole is growing or shrinking, respectively, as documented in Hartvig et al. (2010). The present implementation also rests on the definitions of the scour depth S and scour volume V and their development equation as detailed in Hartvig (2011). The monopile is subjected to either steady current or linear waves that I onwards simply refer to as *current* or *waves*. Far from the pile, the erosion conditions may be either *clear-water* or *live-bed* as defined later. Finally, the bed material is assumed to be non-cohesive uniform soil. By proper modification, the present implementation may be extended to other cases and treat e.g. non-linear waves, combined current and waves, cohesive sediment, graded sediment, other structural geometries and other development equations.

To concretize the approach further, I go from the bed elevation in Fig. 8.6a and its rate in Fig. 8.7a to the field of the bed shear stress in Fig. 8.11a. From a separate thread of existing work, some knowledge of the field for the bed shear stress for nearly the same configuration is known. Both fields of the bed shear stress should approximately agree and this compatibility condition facilitates the investigation of the underlying components or parameters of the reverse approach. Specifically, I investigate the performance of two bed load models and the sensitivity of the time scale on the bed shear stress. In future research, other investigations and even the calibration of the underlying parameters can be undertaken if the approach is found to be sufficiently accurate.

Besides the idea of going backwards in the interaction triangle, the present approach is also unique in that it operates on conventional bed load models. It can therefore be used for benchmarking the bed load models or the studies that are based on them. It also presents a new model for sediment pickup and the entrainment rate based mainly on the friction velocity and the mean grain concentration in the bed load layer. Ultimately, I hope that

the present approach can contribute to advancing the development of a tractable and accurate long-term method for forecasting the scour hole development in typical field conditions.

The rest of the paper is organized as follows: After some opening clarifications, I present the governing equations for the problem. In Secs. 4-5., I use the forward approach to establish the boundary conditions and the reverse approach to establish the field conditions. In Sec. 6, I detail the spatial discretization and present a summary of the main scheme. Finally, in Secs. 7-8, I present the results for one configuration, discuss these and conclude briefly on the findings.

2. Opening clarifications

Before I proceed too far, I would like to introduce the domain, my notation, the identities and numerical methods that I frequently invoke in the paper.

2.1. Domain

The Cartesian and polar coordinate systems are shown in Fig. 8.2. The streamwise axis is denoted by x, the lateral axis by y, the radius from Origo by r and the angle relative to the streamwise axis by $\theta \in [\pi; \pi]$. It is implied that the vertical axis z points upward from Origo.

The bed domain A in the xy-plane is assumed to be composed of the *near-field* domain A_Γ and the *scour domain* A_Ω. The two latter domains are shown in dark and light gray, respectively. The bed domain is bounded by the inner boundary $r = r_{\min}$ and the outer boundary $r = r_\infty$. Since I will here consider a circular pile with the pile axis in Origo, $r_{\min}$ is constant with respect to θ and related to the outer pile diameter $D = 2\ r_{\min}$. For convenience, the outer boundary is taken to be circular too with a constant radius r_∞.

The scour domain A_Ω defines the plane extent of the scour hole and is shaped as a semi-circle upstream $(x > 0)$ and a semi-ellipse downstream $(x > 0)$ as given by Hartvig (2011). The scour domain has the outer radius r_c in the upstream and lateral directions and the outer radius $r_c c_r$ in the downstream direction.

The presence of the pile and the conditions in the scour domain will influence the conditions in the near-field domain. In contrast, the outer boundary is placed sufficiently far away from the pile and the scour domain that it is assumed to be undisturbed by their influence. Consequently, I will refer to the variables at the outer boundary as *undisturbed* and suffix

them with r_∞. The domain outside the bed domain is referred to as the *far-field*.

[Fig. 8.2 about here]

2.2. Notation & Identities

I write a vector in the two-dimensional Euclidean xy-plane as v_α where the subscript α is reserved to denote indices 1 and 2. The Cartesian and polar components are written $(v_x, v_y)_{\text{rec}}$ and $(v_r, v_\theta)_{\text{pol}}$, respectively. The quantities are defined in Fig. 8.2. I note here that I often use the Cartesian components to represent a vector concisely although the numerical scheme operates entirely on the polar components based partly on the following identities. The *magnitude* of the vector is written as v without the tensor index or as $|v_\alpha|$ where the double lines $||$ denote magnitude or absolute value. The vector magnitude is computed in terms of its polar components as:

$$|v_\alpha| = \sqrt{v_r^2 + v_\theta^2} \tag{2.1}$$

In addition, I also adhere to Einstein's summation rule so terms with repeated tensor indices imply summation of the term over each value of the tensor index, i.e. $\partial v_\alpha / \partial x_\alpha \equiv \partial v_x / \partial x + \partial v_y / \partial y$. The previous quantity $\partial v_\alpha / \partial x_\alpha$ is the *divergence* of the vector v_α and is equivalently expressed in polar terms:

$$\frac{\partial v_\alpha}{\partial x_\alpha} = \frac{\partial v_r}{\partial r} + \frac{1}{r}\left(\frac{\partial v_\theta}{\partial \theta} + v_r\right) \tag{2.2}$$

Likewise, I write a three-dimensional Euclidean vector as v_i where the subscript i is reserved to denote indices $1, 2, 3$ and the Cartesian components are denoted $(v_x, v_y, v_z)_{\text{rec}}$.

For illustrative purposes, I use f to represent a general scalar variable and its precise meaning should be clear from the context. The *gradient* vector $\partial f / \partial x_\alpha$ of f is expressed in terms of its polar components:

$$\frac{\partial f}{\partial x_\alpha} = \left(\frac{\partial f}{\partial r}, \frac{1}{r}\frac{\partial f}{\partial \theta}\right)_{\text{pol}} \tag{2.3}$$

2.3. Numerical methods

Turning to the numerical methods:

- *Quadrature* refers here to integration of a known scalar function by the adaptive Simpson's method.
- *Discrete integration* refers here to integration of a discrete signal of a scalar function by the trapezoidal method. By nesting the operation and restating the integrand, the method is also used to integrate a scalar field function over the bed domain by exploiting:

$$\int_A f \; da = \int_{r_{\min}}^{r_\infty} \int_{-\pi}^{\pi} f r \; d\theta \; dr \tag{2.4}$$

  where a is an infinitesimal area of the bed domain A.
- *Finite differences* are used to differentiate a discrete signal of a scalar function or discretize a field function as elaborated in Sec. 6.
- The *bisection method* is used to determine the solution $x_f \in [x_a, x_b]$ that satisfies the implicit equation $f(x_f) = 0$.

3. Governing Equations

In this section, I present the governing equations that I have considered, namely the Exner equation, two bed load models and a model for the entrainment rate that enters the Exner equation. These equations are common for both a forward and reverse approach although the model for the entrainment rate has been developed with the reverse approach in mind.

3.1. Exner equation

If the sediment can be decomposed into a *suspended* and *bed* load and the latter can be regarded as an incompressible continuum, then the conservation of mass or volume of the bed material is expressed by the Exner differential equation:

$$-C_h \frac{\partial h}{\partial t} = \frac{\partial Q_{b\alpha}}{\partial x_\alpha} + e \tag{3.1}$$

In the equation, $\partial h/\partial t$ is the bed elevation rate, h is the bed elevation defined positive upwards from a reference level and t is time. Furthermore, $Q_{b\alpha}$ is the bed load flux and e is the entrainment rate that determines the

transfer to suspended load. In this connection, I want to clarify that $Q_{b\alpha}$ is here the volumetric flux of the bed material in the bed load layer per unit width and e is the volumetric *net* flux in upwards direction per unit area. The latter thus represents entrainment in a general sense that covers both pick-up $(e > 0)$ and deposition $(e < 0)$ of grains. C_h is the volumetric grain concentration in the bed, i.e. the ratio of the grain volume to the bulk volume and lies in the range $]0, C_{\max}]$. $C_{\max}$ is the maximum grain concentration that corresponds to the arrangement of grains that gives least possible pore space.

3.2. Bed load models

In order to expose the influence of the choice of the bed load model, I have implemented two bed load models. I have designed the models mainly on the influential work of Brørs (1999) and Roulund et al. (2005) and consequently, I have allowed myself to refer to the two models as the *Brørs* and *Roulund* model, respectively. Both of these models operate on mean quantities and in the present framework, they can thus only predict mean quantities, such as the bed load flux or the mean bed shear stress. On the following lines, I will describe the common properties of the two models and afterwards, detail each of them.

3.2.1. Common properties

The Shields number is defined as:

$$\zeta' \equiv \frac{\tau'}{(s-1)\,\rho_f g d} \tag{3.2}$$

where ζ' is the Shields number, g is the acceleration due to gravity, d is a characteristic grain diameter, ρ_f is the density of the fluid, $s = \rho_d/\rho_f$ is the relative grain-fluid density and ρ_d is the density of the solid grain. τ'_α is the mean bed shear stress at the bed surface that is induced by the presumingly grain-free fluid. It is also written in terms of the friction velocity:

$$U'_{f\alpha} \equiv \begin{cases} \dfrac{\tau'_\alpha}{\tau'}\sqrt{\dfrac{\tau'}{\rho_f}}, & \tau' > 0 \\ 0, & \text{else} \end{cases} \tag{3.3}$$

where $U'_{f\alpha}$ is the friction velocity vector with the magnitude $U'_f = \sqrt{\tau'/\rho_f}$. The prime $(\,)'$ denotes the contribution from *skin friction*. When the bed is hydraulically rough and one has smeared out the effect of the roughness

elements in the simulation or experiment rather than resolving them in detail, the apparent bed shear stress τ and the related quantities U_f and ζ will include an additional contribution from *form drag* and this contribution is thus neglected in (3.2).

For the present problem, the bed elevation can vary considerably in space and it becomes important to include the influence of the slope. From analytical geometry, the slope angle is:

$$\phi = \tan^{-1}\left|\frac{\partial h}{\partial x_\alpha}\right| \tag{3.4}$$

where $\phi \geq 0$ is the slope angle that is computed using (2.1), (2.3) and (3.4) with the polar derivatives given by Sec. 6.2. The slope angle is zero for a locally plane bed and can attain a maximum value equal to the repose angle ϕ_r. The latter is related to the static coefficient of friction μ_s by $\mu_s = \tan\phi_r$. Following Roulund et al. (2005), the critical Shields number is computed as:

$$\zeta_c = \zeta_{c0} \cdot \left(\cos(\phi)\sqrt{1 - \frac{\sin^2(\theta_3)\tan^2(\phi)}{\mu_s^2}} - \frac{\cos(\theta_3)\sin(\phi)}{\mu_s}\right) \tag{3.5}$$

where ζ_c is the critical Shields number, ζ_{c0} is the critical Shields number for a plane bed and θ_3 is the angle defined in Fig. 8.3. If the bed is plane or τ' is zero, the angles θ_3 to θ_5 are not defined by Fig. 8.3, but are all taken as zero. In this connection, the angle θ_2 is often helpful and can be determined by exploiting (2.3) and Figs. 8.2–8.3 as:

$$\theta_2 = \text{atan2}\left(y_2 = -\frac{1}{r}\frac{\partial h}{\partial \theta}, x_2 = -\frac{\partial h}{\partial r}\right) \tag{3.6}$$

where $\text{atan2}(y_2, x_2)$ is the two-argument arctangent function in the range $[-\pi, \pi]$, in contrast to the conventional one-argument arctangent function $\tan^{-1}(y_2/x_2)$ in the range $]-\pi/2, \pi/2[$ that is used in (3.4).

The quantity $\zeta' - \zeta_c$ is central for characterizing the bed load flow. To be concise, I refer to the situation $\zeta' < \zeta_c$ as *subcritical*, $\zeta' = \zeta_c$ as *critical* and $\zeta' > \zeta_c$ as *supercritical*.

[Fig. 8.3 about here]

3.2.2. The Brørs model

Following Brørs (1999), the bed load flux of the Brørs model is taken as:

$$Q_{b\alpha} = \begin{cases} Q_{b0} \cdot \left(\dfrac{\tau'_\alpha}{\tau'} - c_Q \dfrac{\partial h}{\partial x_\alpha} \right), & \zeta' > \zeta_c \\ 0, & \text{else} \end{cases} \tag{3.7}$$

where Q_{b0} is the magnitude of the bed load flux in case of plane bed and c_Q is a slope coefficient. If the bed is plane or $c_Q = 0$, the second term on the upper right-hand-side of (3.7) vanishes, meaning that the bed load flux will have the magnitude Q_{b0} and be directed in the same direction as the bed shear stress. In other cases, the bed load flux will have a different magnitude from Q_{b0} and be directed somewhere between the directions of the shear stress and the steepest slope $-\partial h/\partial x_\alpha$, controlled by the slope coefficient c_Q.

Following Brørs (1999), the magnitude of the bed load flux Q_{b0} is determined by the bed load equation of Nielsen (1992, Sec. 2.3.4):

$$Q_{b0} = 12 \ \left(\zeta' - \zeta_c\right) \sqrt{\zeta'} \sqrt{(s-1) g d^3} \tag{3.8}$$

Deviating slightly from Brørs (1999), the equilibrium grain concentration in the bed load layer is determined from the following piece-wise lines:

$$C_{be} = \begin{cases} 0, & \zeta' \leq \zeta_c \\ 0.30 \dfrac{\zeta' - \zeta_c}{0.75 - \zeta_c}, & \zeta_c < \zeta' < 0.75 \\ 0.30, & 0.75 \leq \zeta' \end{cases} \tag{3.9}$$

where C_{be} is the equilibrium mean grain concentration in the bed load layer.

3.2.3. The Roulund model

The Roulund model is based on the approach of Roulund et al. (2005) that is a two-dimensional generalization of the bed load equation of Engelund and Fredsøe (1976). The bed load flux is given as:

$$Q_{b\alpha} = U_{b\alpha} p d \frac{\pi}{6} \tag{3.10}$$

where $U_{b\alpha}$ is the bed load velocity and $p \in [0, 1]$ is the ratio between the actual and maximum amount of grains that are traveling as bed load. This function is given as:

$$p = \begin{cases} \left(1 + \left(\frac{\frac{\pi}{6}\mu_d}{\zeta' - \zeta_c}\right)^4\right)^{-1/4}, & \zeta' > \zeta_c \\ 0, & \text{else} \end{cases} \tag{3.11}$$

where μ_d is the dynamic coefficient of friction, fulfilling $\mu_d < \mu_s$. The relation between $U_{b\alpha}$ and τ'_α is obtained from the following considerations. Imagine a single spherical grain as it travels in the bed load layer with presumingly constant speed along a linear path. The grain is assumed to be subjected only to the forces of gravity, buoyancy, fluid drag and friction, given by:

$$\begin{aligned} F_g &= \frac{\pi}{6} d^3 \rho_f g \cdot (s-1) \\ F_D &= \frac{\pi}{4} d^2 \frac{1}{2} \rho_f c_D U_{\text{rel}}^2 \\ F_\mu &= \mu_d F_{g \perp x'} \end{aligned} \tag{3.12}$$

Above, F_g is the gravity force in downwards direction reduced by hydrostatic buoyancy, F_D is the fluid drag force in the direction of the relative velocity and F_μ is the friction force in the opposite direction of motion. U_{rel} is the magnitude of the relative velocity, c_D is a drag coefficient. and $F_{g \perp x'}$ is the reduced gravity force normal to the steepest bed slope. The relative velocity is defined by:

$$U_{\text{rel}\alpha} \equiv c_u U'_{f\alpha} - U_{b\alpha} \tag{3.13}$$

where $U_{\text{rel}\alpha}$ is the relative velocity and c_u is an amplification coefficient that determines the ratio of the mean fluid velocity in the bed load layer to the friction velocity. The drag coefficient is computed as:

$$c_D = \frac{8\mu_d}{3c_u^2 \zeta_{c0}} \tag{3.14}$$

The reduced gravity force F_g can be decomposed into the direction of the steepest bed slope and normal to the steepest bed slope:

$$\begin{pmatrix} F_{g \parallel x'} \\ F_{g \perp x'} \end{pmatrix} = F_g \cdot \begin{pmatrix} \sin\phi \\ \cos\phi \end{pmatrix} \tag{3.15}$$

where $F_{g \parallel x'}$ is the reduced gravity force in the direction of the steepest bed slope. Following Newton's 1st law, the external static forces in the direction of particle motion must be in equilibrium:

$$F_{g\|x'}\cos(\theta_3-\theta_4)+F_D\cos\theta_5-F_\mu=0 \tag{3.16a}$$

where the angles θ_4 and θ_5 are illustrated in Fig. 8.3. By considering the forces normal to the particle direction and the geometrical relations of the relative velocity according to (3.13) and Fig. 8.3, three additional equations can be obtained:

$$-F_{g\|x'}\sin(\theta_3-\theta_4)+F_D\sin\theta_5=0 \tag{3.16b}$$

$$U_{\text{rel}}\sin\theta_5-c_uU_f'\sin\theta_4=0 \tag{3.16c}$$

$$U_{\text{rel}}\cos\theta_5-c_uU_f'\cos\theta_4+U_b=0 \tag{3.16d}$$

If the bed is plane ($\phi=\theta_3=\theta_4=\theta_5=0$) and the Shields number is supercritical, Eqs. (3.16a) and (3.16d) yield $U_b=c_uU_f'\cdot(1-\sqrt{\zeta_c/(2\zeta')})$ in the direction of the fluid velocity. For small Shields numbers, we further obtain $p\simeq(\zeta'-\zeta_c)/(\mu_d\pi/6)$ as seen from (3.11). In this case, Eq. (3.10) reduces to the more familiar version of the Engelund and Fredsøe (1976) bed load equation:

$$Q_{b0}\simeq\begin{cases}\dfrac{c_u}{\mu_d}\,(\zeta'-\zeta_c)\left(\sqrt{\zeta'}-0.7\,\sqrt{\zeta_c}\right)\sqrt{(s-1)gd^3}, & \zeta'>\zeta_c\\ 0, & \text{else}\end{cases} \tag{3.17}$$

that bears a resemblance to the Nielsen (1992) equation in (3.8). Roulund et al. (2005) did not treat the suspended load and therefore did not assume a model for the equilibrium grain concentration in the bed load layer. Instead, C_{be} is here taken from Engelund and Fredsøe (1976) based partly on Bagnold (1954):

$$C_{be}=\begin{cases}\dfrac{C_{\max}}{\left(1+C_l^{-1}\right)^3}, & \zeta'-\zeta_c-\frac{\pi}{6}\mu_dp>0\\ 0, & \text{else}\end{cases} \tag{3.18}$$

where C_l is the corresponding linear grain concentration. This is given as:

$$C_l=\sqrt{\frac{\zeta'-\zeta_c-\dfrac{\pi}{6}\mu_dp}{c_ls\zeta'}} \tag{3.19}$$

where c_l is a coefficient for the sediment-fluid flow. For large Shields numbers, we obtain $p \simeq 1 \Rightarrow C_l \simeq (c_l s)^{-1/2}$ and with the typical choices $c_l = 0.027$, $s = 2.65$ and $C_{\max} = 0.65$ for natural sediments in a fluid with a logarithmic velocity profile near the bed, the equilibrium grain concentration in the bed load layer approaches the asymptotic limit $C_{be} \simeq 0.32$. This is comparable to the maximum limit of the Brørs model in (3.9), $C_{be} \simeq 0.30$.

3.3. Entrainment rate

In this section, I describe the entrainment rate e that enters the Exner equation and develop a model for it, inspired partly by Garcia and Parker (1991), Rijn (1985) and Engelund and Fredsøe (1976).

If the suspended load can be regarded as an incompressible continuum and the fluid velocity and the grain concentration can be decomposed into mean and fluctuating contributions, the Reynolds-averaged equation for the conservation of mass or volume of the suspended load is:

$$\frac{\partial C}{\partial t} + \frac{\partial q_{si}}{\partial x_i} = 0, \quad t > 0 \tag{3.20a}$$

where

$$q_{si} = C \cdot (U_i - W_d \delta_{i3}) + \overline{\tilde{c}\tilde{u}_i} \tag{3.20b}$$

Above, $C, \tilde{c}$ are the mean and fluctuating contributions of the instantaneous volumetric grain concentration, respectively, and similarly, $U_i, \tilde{u}_i$ are the mean and fluctuating contributions of the instantaneous fluid velocity. Furthermore, q_{si} is the mean flux of the grain concentration, W_d is the settling speed of the sediment, δ is the Kronecker delta and the overbar $\overline{(\,)}$ denotes Reynolds averaging. Eqs. (3.20) neglect molecular diffusion since the turbulent fluctuations are considered to be dominant.

If the mass or volume of bed material is conserved and the domain of the transport equation (3.20a) is bounded from below by the upper surface of the bed load layer at the elevation z_b, we must require that the upward flux at this boundary is equal to the entrainment rate:

$$e = q_{sz}(z = z_b) \tag{3.21}$$

If the bed is impermeable, the mean upward fluid velocity must vanish at the bed, i.e. $W(z = 0) = 0$. The mean upward fluid velocity at the boundary between the domains of the bed load and suspended load is therefore assumed to be negligible, i.e. $W(z = z_b) \simeq 0$. This approximation reduces (3.21) to:

$$e \simeq -C_b W_d + \overline{\tilde{c}\tilde{w}}(z = z_b) \tag{3.22}$$

where C_b is the mean grain concentration in the bed load layer. The quantity $\overline{\tilde{c}\tilde{w}}(z = z_b)$ is central to the problem and I will refer to it as the *entrainment correlation*. An equilibrium situation can arise when the entrainment rate is zero. This occurs when the grain concentration is steady and uniform in the xy directions, or the bed surface is steady and the bed load flux is uniform in the xy-plane as seen from (3.1). In this equilibrium situation, $e = 0$ and (3.22) implies:

$$\overline{\tilde{c}\tilde{w}}(z = z_b, e = 0) = C_{be} W_{de} \tag{3.23}$$

where C_{be} is the equilibrium grain concentration in the bed load layer that can be related to Eqs. (3.9) or (3.18)–(3.19). W_{de} is the settling speed in the equilibrium situation. Based on these considerations, I note two simple constraints for the entrainment rate or the entrainment correlation:

1. In the equilibrium situation, the entrainment rate must be zero.
2. In the equilibrium situation, the entrainment correlation must be equal to $C_{be} W_{de}$ as seen from (3.23).

On the next few lines, three models for the entrainment rate or entrainment correlation are considered. Garcia and Parker (1991) proposed that the entrainment correlation is modeled as:

$$\overline{\tilde{c}\tilde{w}}(z = z_b) = C_{be} W_{de} \tag{3.24}$$

In other words, they suggest that the entrainment correlation *in general*, or more precisely in weakly disequilibrium situations, behaves as in the equilibrium situation. This model naturally satisfies the second constraint and allows the first constraint to be satisfied. However, the problem with using it within the present context is the fact that in order to determine the entrainment rate from (3.22), the actual grain concentration in the bed load layer C_b must be determined. This is usually done by solving (3.20a) and evaluating its solution at the boundary. If one simply assumes $C_b = C_{be}$ here, the entrainment rate is erroneously nil at all times.

Dey and Debnath (2001) proposed the following equation for sediment entrainment:

$$\Phi_p = 0.0006 Z' D_*^{0.24} \sigma_d^{1.9}, \quad Z' = \frac{\zeta'}{\zeta_c} - 1 \tag{3.25}$$

where Φ_p is the Einstein entrainment number, Z' is the transport stage and D_*, σ_d are dimensionless coefficients for sediment-fluid properties and grain size distribution, respectively. The Einstein entrainment number is defined as:

$$\phi_p \equiv \frac{E_*}{\rho_d \sqrt{(s-1)\, g d}} \tag{3.26}$$

where E_* is the entrained sediment-mass rate. Based on the usage of this model in Dey and Barbhuiya (2005) and deviating slightly from Yanmaz (2006), one may interpret that E_* is related to the entrainment rate e through $e = E_*/\rho_d$. Then, according to Eqs. (3.25)–(3.26), we always have $e > 0$ when $T > 0$. This interpretation of the model fails to satisfy the first constraint at the outer boundary when live-bed scour occurs ($T > 0$) in an equilibrium situation ($e = 0$).

On the other hand, one can argue that the previous interpretation is incorrect and that a correct interpretation instead relates E_* to the entrainment correlation, i.e.:

$$\overline{\tilde{c}\tilde{w}}(z = z_b) = \frac{E_*}{\rho_d} \tag{3.27}$$

This interpretation also appears to be consistent with the definitions of Rijn (1985, Sec. 4) when bearing in mind that he dealt with the *mass* grain concentration. The interpretation (3.27) allows the first constraint to be satisfied. To satisfy the second constraint, the equilibrium grain concentration must be modeled as $C_{be} = E_* / (\rho_d W_{de})$ instead of using Eqs. (3.9) or (3.18)–(3.19). It is now apparent that this interpretation is equivalent to the Garcia and Parker (1991) model with a particular formulation for C_{be} – and the problem of determining the grain concentration C_b without resorting to solving its transport equation still remains.

Instead, I propose the following model for the entrainment correlation:

$$\overline{\tilde{c}\tilde{w}}(z = z_b) = c_e C_b U'_f \tag{3.28}$$

where c_e is a dimensionless coefficient that I will call the *equilibrium coefficient*. In this model, C_b and U'_f are assumed to be the governing quantities for characterizing the entrainment correlation. The friction velocity associated with skin friction U'_f is retained since it is assumed to be proportional to the total friction velocity U_f and the latter is known to characterize the intensity of the fluctuation $\tilde{w}$ in the inner region of simple boundary layers in the limit of infinite Reynolds number, i.e. $U'_f \propto U_f \propto \sqrt{\overline{\tilde{w}^2}}$. The mean

grain concentration is retained based on the hypothesis that the inertia of the grains is relatively weak so turbulent eddies will convect the available grains at a particular point. Depending on whether there are few or many grains available, on average, the fluctuation $\tilde{c}$ is expected to vary weakly or strongly, respectively, i.e. $\sqrt{\overline{\tilde{c}^2}} \propto C_b$.

The model has several attractive properties. First, the model is dimensionally correct since U_f' appears exactly in the first power in (3.28). Secondly, it allows an independent determination of C_b since C_b appears exactly in the first power in (3.28). By combining Eqs. (3.22), (3.28) and $e = 0$, C_b simply cancels out from the resulting equation:

$$c_e = \frac{W_{de}}{U_{fe}'} \tag{3.29}$$

where U_{fe}' is the friction velocity in the situation of equilibrium entrainment. C_b can therefore be determined from other sources. For the sake of simplicity, I determine it from Eqs. (3.9) or (3.18)–(3.19) by assuming:

$$C_b \approx C_{be} \tag{3.30}$$

This approximation does not imply $e = 0$ at all times as it did in the model of Garcia and Parker (1991). In fact, the present model facilitates both a crude and refined determination of C_b, the former approach based on (3.30) and the latter based on solving and evaluating (3.20). Thirdly, if the equilibrium coefficient is computed from (3.29), both constraints are satisfied. Fourth, (3.29) can be interpreted as a criterion for the onset of entrainment or, in other words, initiation of suspension. As such, it closely resembles the existing empirical criteria of the type $c_{e2} = W_d/U_f'$ where the constant is taken as $c_{e2} = 0.8$ in Engelund and Fredsøe (1976) or $0.25 < c_{e2} < 1$ as summarized in Rijn (1984b). The equilibrium coefficient is also seen to be related to the Rouse number $W_d/(U_f'\kappa)$, where κ is the Karman constant. Finally, the prediction of the present model does not appear to differ radically from the existing models. Using (3.26)–(3.28), the present model can be expressed in terms of the Einstein number as:

$$\Phi_p = c_e C_b \sqrt{\zeta'} \tag{3.31}$$

To illustrate the prediction further, I have exemplified the entrainment correlation $\overline{\tilde{c}\tilde{w}}(z = z_b)$ in Fig. 8.4. It is shown as function of the transport stage Z' for the configuration in Table 8.1 in case of plane bed ($\zeta_c = \zeta_{c0}$), equilibrium condition ($C_b = C_{be}$), $\sigma_d = 1.2$ and $c_u = 10$. The reported

formulas for the Einstein number Φ_p of Dey and Debnath (2001) in (3.25) and Rijn (1984d) have been related to the entrainment correlation through (3.26)–(3.27). The Garcia and Parker (1991) model of (3.24) is shown using the settling speed of a solitary grain as given by (3.32). Furthermore, three different formulations of the equilibrium grain concentration C_{be} have been used where the suffixes Br, Ro and Ri refer to C_{be} based on the Brørs model (3.9), Roulund model (3.18)–(3.19) or the model of Rijn (1984b), respectively. The present model is shown using the equilibrium grain concentration assumption (3.30) and prescribing the equilibrium coefficient $c_e = 0.4$ rather than computing it from (3.29). The figure indicates that the order of magnitude of the entrainment correlation is comparable for all the models for the considered range of the transport stage.

Following Fredsøe and Deigaard (1992, pp. 198-200), the settling speed for a *solitary* grain in a still fluid is given by the following equation:

$$W_{d0} = \sqrt{\frac{4\,(s-1)\,gd}{3C_{D2}}}, \quad C_{D2} = 1.4 + \frac{36}{R_2}, \quad R_2 = \frac{W_{d0}d}{\nu} \tag{3.32}$$

where C_{D2} is a drag coefficient, R_2 is a Reynolds number, W_{d0} is the settling speed in the case of a solitary grain and the implicit equation is solved by the bisection method. The settling speed of the sediment W_d in the presence of *neighboring* grains may be less than W_{d0} depending on the grain concentration. As an approximation, the dependence on the grain concentration is entirely neglected and the results from the case of a solitary grain are used at all times, i.e.:

$$W_d \approx W_{de} \approx W_{d0} \tag{3.33}$$

Combining Eqs. (3.22), (3.28), (3.29), (3.30) and (3.33), the entrainment rate is in practice computed as:

$$e = W_d C_{be} \cdot \left(\frac{U'_f}{U'_{fe}} - 1 \right) \tag{3.34}$$

[Fig. 8.4 about here]

4. Boundary Conditions

Based on the existing knowledge on the bed shear stress in undisturbed boundary layer flows and the governing equations from the previous section, I will derive the conditions at the inner and outer boundary in this section. Due to the complexity of the numerical scheme, my presentation is bound to become more detailed from this point on. The reader is encouraged to review Sec. 6.4 from time to time to obtain an overview of the scheme in its entirety.

4.1. Bed shear stress

If the current or waves are traveling in the streamwise direction x, the undisturbed mean bed shear stress is one-dimensional and is taken as:

$$\tau'_\alpha\big|_{r_\infty} = \begin{pmatrix} \tau'_x\big|_{r_\infty} \\ 0 \end{pmatrix}_{\text{rec}} \tag{4.1}$$

where $\tau'_x|_{r_\infty}$ is the component in the streamwise direction that I call the *streamwise bed shear stress* and determine from relevant boundary layer theories.

For current, the streamwise bed shear stress is determined from the Colebrook-White equation that is valid for the boundary layer flows in pipes and channels with steady mean current:

$$\tau'_x|_{r_\infty} = \frac{\rho_f f'_{cu} U_{cu}^2}{2}, \quad f'_{cu} = \frac{f'_d}{4}, \quad \frac{1}{\sqrt{f'_d}} = -2\log_{10}\left(\frac{k_N}{3.7D_e} + \frac{2.51}{R_e\sqrt{f'_d}}\right), \quad R_e = \frac{U_c D_e}{\nu} \tag{4.2}$$

Above, f'_{cu} is the friction factor for current, U_{cu} is the depth-averaged fluid velocity in the streamwise direction and D_e is the equivalent pipe diameter. The equation is solved by the bisection method.

For waves, the streamwise bed shear stress is determined by an adjustment of the results for oscillatory boundary layers. Oscillatory boundary layers experience a harmonic temporal variation that can be expressed as:

$$\tau'_x\big|_{r_\infty} = \tau'_m \cos(\omega t + \xi)$$

Above, τ'_m is the magnitude of the bed shear stress, $\omega = 2\pi/T$ is the circular wave period, T is the wave period and ξ is the phase advance of the bed shear stress compared to the streamwise fluid velocity. To facilitate a spatial variation that resembles the wave flow according to linear wave

theory, I adjust the above equation by introducing a spatial term in the argument of the cosine function and compute the streamwise bed shear stress as:

$$\tau_x'\big|_{r_\infty} = \tau_m' \cos\left(\omega t - kx + \xi\right) \tag{4.3}$$

where $k = 2\pi/L$ is the wave number, L is the wave length and the minus in the spatial term mimics that the wave is propagating in the x-direction. The remaining results from the theory of oscillatory boundary layer are left unchanged. The parameters of Sec. 7 suggest that the boundary layer is laminar throughout the wave cycle at the outer boundary and for laminar oscillatory boundary layers, the bed shear stress magnitude is:

$$\tau_m' = \frac{\rho_f \nu U_m}{\sqrt{\frac{\nu}{\omega}}} \tag{4.4}$$

where U_m is the magnitude of the streamwise fluid velocity close to the bed but above the boundary layer. If the boundary layer at the outer boundary is transitional or predominantly turbulent, τ_m' can be determined from other expressions, see e.g. Fredsøe and Deigaard (1992).

Finally, I will introduce some definitions for the undisturbed parameters for later use. The reference bed shear stress τ_{ref}' is:

$$\tau_{\text{ref}}' = \begin{cases} \tau_x'\big|_{r_\infty}, & \text{Current} \\ \tau_m', & \text{Waves} \end{cases}$$

and the corresponding reference Reynolds number is:

$$R_{\text{ref}} = \begin{cases} U_{cu} D/\nu, & \text{Current} \\ U_m D/\nu, & \text{Waves} \end{cases}$$

Depending on whether the corresponding reference Shields number is subcritical or supercritical, the far-field is characterized as being in the state of clear-water or live-bed.

4.2. Bed load flux

Once the undisturbed bed shear stress has been determined as outlined above, the undisturbed bed load flux $Q_{b\alpha}\big|_{r_\infty}$ can be determined. In practice, the undisturbed bed is assumed to be plane or approximately plane, such that the undisturbed bed load flux is one-dimensional as the bed shear stress. For subcritical or critical Shields number, I take $Q_{b\alpha}\big|_{r_\infty} = 0$. For supercritical Shields number, I determine the sign of bed load flux as that of

$\tau'_x|_{r_\infty}$ and determine the bed load flux magnitude from either (3.8) or (3.17) depending on which model is active.

The bed load flux must also satisfy the boundary conditions at the inner and outer boundary. The inner boundary is assumed to be impermeable and therefore, the bed load flux normal to the pile perimeter must be zero. At the outer boundary, the bed load flux must be identical to the undisturbed one. This can be expressed as:

$$Q_{b\alpha} n_\alpha = 0, \quad r = r_{\min} \tag{4.5a}$$

$$Q_{b\alpha} = \left(Q_{bx}|_{r_\infty}, 0 \right)_{\text{rec}}, \quad r = r_\infty \tag{4.5b}$$

where n_α is the normal vector of the inner boundary. These boundary conditions are put into use when the bed load flux within the bed domain is to be determined.

4.3. Entrainment rate

Once the undisturbed bed shear stress and undisturbed bed load flux have been determined, the corresponding undisturbed grain concentration in the bed load layer C_{be} is determined from Eqs. (3.9) or (3.18)–(3.19). To compute the undisturbed entrainment rate from (3.34), it is now necessary to determine the equilibrium friction velocity U'_{fe}.

For current, the undisturbed entrainment rate must be zero as discussed previously in Sec. 3.3 and the equilibrium friction velocity is therefore taken as the undisturbed friction velocity, i.e.:

$$e|_{r_\infty} = 0 \quad \Leftrightarrow \quad U'_{fe} = U'_f\Big|_{r_\infty} \tag{4.6}$$

For waves, the equilibrium friction velocity U'_{fe} is determined implicitly by requiring that the *period-average* of the undisturbed entrainment rate is nil, i.e.:

$$\langle e \rangle|_{r_\infty} = 0 \quad \Leftrightarrow \quad U'_{fe} \tag{4.7}$$

where the brackets $\langle\rangle$ denote the period-average. The period-average is defined by the following operation:

$$\langle f \rangle \equiv \frac{1}{T} \int_0^T f \, dt$$

where f is the scalar function that is to be averaged. Eq. (4.7) is solved by the bisection method and the obtained solution for U'_{fe} is always slightly smaller than the maximum undisturbed friction velocity $\sqrt{\tau'_m/\rho_f}$.

The rationale for the above choice is given on the following lines by studying the period-average of the Exner equation (3.1):

$$\langle -C_h \frac{\partial h}{\partial t} \rangle = \langle \frac{\partial Q_{b\alpha}}{\partial x_\alpha} \rangle + \langle e \rangle \tag{4.8}$$

The order of differentiation and integration can be interchanged and if the grain concentration in the bed C_h is constant with respect to time, (4.8) reduces to:

$$-C_h \frac{\partial \langle h \rangle}{\partial t} = \frac{\partial \langle Q_{b\alpha} \rangle}{\partial x_\alpha} + \langle e \rangle \tag{4.9}$$

Now consider an arbitrary point P at the outer boundary as time passes. The temporal development of the bed shear stress from (4.3) reveals that its period-average must be zero, i.e. $\langle \tau'_x \rangle|_P = 0$. If the undisturbed bed is also approximately plane, the period-average of (3.8) or (3.17) is also nil, i.e. $\langle Q_{bx} \rangle|_P \approx 0$. Next, the period-average of the undisturbed bed is assumed to be steady, i.e. $\langle h \rangle|_P = 0$. Then, it is apparent from Eq. (4.9) that the period-averaged entrainment rate must be zero too, $\langle e \rangle|_P = 0$.

4.4. Bed elevation rate

The undisturbed bed elevation rate can now be found by considering the Exner equation at the outer boundary:

$$\frac{\partial h}{\partial t} = \frac{1}{-C_h} \left(\frac{\partial Q_{b\alpha}}{\partial x_\alpha} + e \right), \quad r = r_\infty \tag{4.10}$$

For both current and waves, the undisturbed bed elevation can be determined as the right-hand-side of (4.10). Based on the arguments from the previous sections, I note here that $(\partial h/\partial t)|_{r_\infty} = 0$ for current. For waves, the undisturbed bed elevation rate is not necessarily zero since there may be a contribution from the bed load flux divergence or the entrainment rate. In this case, the undisturbed divergence is computed by (2.2) with the derivatives from Sec. 6.2 and the polar components $(Q_{br}, Q_{b\theta})_{\text{pol}} = Q_{bx}|_{r_\infty} \cdot (\cos\theta, -\sin\theta)_{\text{pol}}$.

5. Field Conditions

Having now presented the governing equations and the boundary conditions, it is now time to move on to the field conditions. Since these steps are not trivial, I would like to pause for a moment and give an overview of the rationale here with reference to the Exner equation (3.1). As seen from the equation, it describes the relation between the grain concentration in the bed C_h, the bed elevation rate $\partial h/\partial t$, the bed load flux divergence $\partial Q_{b\alpha}/\partial x_\alpha$ and the entrainment rate e at each point in the bed domain. The procedure to determine the bed shear stress in the bed domain therefore involves the following six assumptions or steps:

1. First, C_h is assumed to be known and constant with respect to time and space.
2. Secondly, $\partial h/\partial t$ is prescribed in the bed domain such that it resembles that of Hartvig (2011) in the scour domain and approaches the undisturbed bed elevation rate at the outer boundary as given by (4.10).
3. Now, the only remaining unknown in (3.1) is the bed load flux $Q_{b\alpha}$ since its divergence and the entrainment rate can both be considered to be functions of $Q_{b\alpha}$. To proceed, a guess $\hat{e}$ is made of the true field of the entrainment rate e such that the guessed entrainment rate approaches the undisturbed value at the outer boundary as given in Sec. 4.3 and satisfies a volume rate condition as detailed later. The hat $\widehat{(\,)}$ denotes *guess*.
4. Fourth, the bed load flux is assumed to be irrotational so the Exner equation simplifies to the Poisson equation. By approximating the derivatives of the Poisson equation and its boundary conditions with finite differences, the resulting matrix equation can be solved and the bed load flux in the bed domain can be determined as detailed later.
5. Fifth, since the bed load flux is now known, one of the bed load models can be used to determine the friction velocity and the grain concentration in the bed load layer. Subsequently, the field of the entrainment rate can be computed by (3.34) and is denoted e_*.
6. Since the guessed $\hat{e}$ and computed e_* fields of the entrainment rate should be identical, steps 3–5 are repeated until acceptable agreement has been achieved.

5.1. Bed elevation rate

The bed elevation rate is decomposed into two contributions:

$$\frac{\partial h}{\partial t} = \left(\frac{\partial h}{\partial t}\right)_* + \left(\frac{\partial h}{\partial t}\right)_{**} \tag{5.1}$$

where the first contribution represents the contribution of Hartvig (2011) and the last represents a modification. The two contributions are referred to as the *unmodified* and *modified* bed elevation rate, respectively. For later uses, I define the volume rate of each contribution as:

$$-\frac{dV}{dt} \equiv \int_A \left(\frac{\partial h}{\partial t}\right)_* da, \quad M \equiv \int_A \left(\frac{\partial h}{\partial t}\right)_{**} da, \tag{5.2}$$

where dV/dt and M are referred to as the *scour volume rate* and the *modified volume rate*, respectively. Both $(\partial h/\partial t)_*$ and dV/dt are given as input in the present scheme.

On the following lines, I will detail how the modified bed elevation rate and its volume rate is determined. For current, a bank of deposited bed material can appear downstream of the scour hole. In this case, M is prescribed and the bank rate is taken to be a hemiellipsoid with the origin in the point $(x_h = r_c c_r + r_h, 0)_{\text{rec}}$, the radius r_h in the xy-plane and the height r_z, i.e.:

$$\left(\frac{\partial h}{\partial t}\right)_{**} = \begin{cases} r_z \cdot \sqrt{1 - \left(\frac{r_3}{r_h}\right)^2}, & r_3 < r_h \\ 0, & \text{else} \end{cases} \tag{5.3}$$

where $r_3 = \sqrt{(x - x_h)^2 + y^2}$ is a relative radius. The upper equation of (5.3) has been obtained from the canonical definition of an ellipsoid with offset, i.e. $\left((x - x_h)/r_x\right)^2 + (y/r_y)^2 + (z/r_z)^2 = 1$. The height is computed as:

$$r_z = 3M/(2\pi r_h^2)$$

to ensure that the volume of the bank rate is exactly M. For waves, the modified bed elevation is prescribed similar to the undisturbed values:

$$\left(\frac{\partial h}{\partial t}\right)_{**} = \frac{1}{-C_h}\left(\left.\frac{\partial Q_{b\alpha}}{\partial x_\alpha}\right|_{r_\infty} + e|_{r_\infty}\right) \tag{5.4}$$

where $(\partial Q_{b\alpha}/\partial x_\alpha)|_{r_\infty}$ and $e|_{r_\infty}$ should be interpreted as the undisturbed values at the same streamwise position x as the field point in consideration. Following the definition in the right equation of (5.2), M is then computed by discrete integration of (5.4) over the bed domain.

5.2. Bed load flux

If $\partial Q_{by}/\partial x = \partial Q_{bx}/\partial y$, the bed load flux can be assumed to be irrotational in the mathematical sense. In this case, the bed load flux can be expressed as the gradient of a scalar function:

$$Q_{b\alpha} = \frac{\partial \Lambda}{\partial x_\alpha} \tag{5.5}$$

where Λ is a scalar field function that I refer to as the *potential*. Turning to the Exner equation (3.1), it can be interpreted as a field condition. By assuming the irrotational hypothesis (5.5) and applying the polar expression for divergence (2.2) and gradient (2.3), the field condition is restated in polar terms as:

$$\frac{\partial^2 \Lambda}{\partial r^2} + \frac{1}{r}\frac{\partial \Lambda}{\partial r} + \frac{1}{r^2}\frac{\partial^2 \Lambda}{\partial \theta^2} = -C_h \frac{\partial h}{\partial t} - e, \quad r_{\min} < r < r_\infty \tag{5.6a}$$

where the left-hand-side represents the divergence $\partial Q_{b\alpha}/\partial x_\alpha$ of the bed load flux or the Laplacian $\partial^2 \Lambda/\partial x_\alpha^2$ of the potential. The boundary conditions (4.5) are also restated in polar terms:

$$\frac{\partial \Lambda}{\partial r} = 0, \quad r = r_{\min} \tag{5.6b}$$

$$\frac{\partial \Lambda}{\partial r} = Q_{bx}|_{r_\infty} \cos\theta, \quad r = r_\infty \tag{5.6c}$$

In formulating these boundary conditions, it has been assumed that the undisturbed bed is approximately plane. It has also been exploited that the pile perimeter and the outer boundary are both circular and have the normal vector $n_\alpha = (\cos\theta, \sin\theta)_{\text{rec}}$.

If we turn to the field for the entrainment rate e on the right-hand-side of Eq. (5.6a) and for a moment perceive it to be known, the system of equations in (5.6) can be interpreted as the Poisson equation in Λ with two Neumann boundary conditions. Such a problem can be solved by discretizing it and solving the resulting system of linear equations.

If we return to reality, the field for the entrainment rate is unknown. In the present formulation with the bed load flux governed by either the Brørs or Roulund model, the entrainment rate depends non-linearly on the bed load flux magnitude Q_b and thus on its potential Λ. Even if the entrainment rate did depend linearly on the bed load flux magnitude, it would still depend non-linearly on the potential. This non-linearity rules out an explicit determination of the entrainment rate.

Therefore, the entrainment rate is determined implicitly by guessing the field by iteration as detailed in Sec. 5.5. For each guessed field, the system of equations in (5.6) is updated and solved for Λ as described in Sec. 6.3 and the corresponding bed load flux $Q_{b\alpha}$ is computed by (2.3) and (5.5) with the polar derivatives approximated as detailed in Sec. 6.2.

5.3. Volume rate condition and bed load outflux

Besides the Exner equation, an additional condition must be satisfied that I derive here. Integration of the Exner equation over the bed domain A gives:

$$-\int_A C_h \frac{\partial h}{\partial t}\, da = \int_A \frac{\partial Q_{b\alpha}}{\partial x_\alpha}\, da + \int_A e\, da, \quad t > 0 \tag{5.7}$$

The individual terms in equation (5.7) can be rewritten in a more concise form. In addition to (5.2), the following two definitions are introduced:

$$F \equiv \int_A \frac{\partial Q_{b\alpha}}{\partial x_\alpha}\, da, \quad E \equiv \int_A e\, da \tag{5.8}$$

where F is the bed load outflux and E is the entrained outflux. The quantities express the volume rate at which the bed material leaves the bed domain as bed or suspended load, respectively. If the grain concentration in the bed is constant with respect to the bed domain, (5.7) reduces to the following *volume rate condition*:

$$C_h \cdot \left(M - \frac{dV}{dt}\right) + F + E = 0 \tag{5.9}$$

By exploiting the divergence theorem, the bed load outflux F can be expressed entirely in terms of the undisturbed bed load flux and the normal vector of the outer boundary:

$$F = \int_C Q_{b\alpha} n_\alpha\, dc = 2\int_0^\pi Q_{bx}\left(\theta, r = r_\infty\right) \cos\left(\theta\right) r_\infty\, d\theta \tag{5.10}$$

where dc is an infinitesimal piece of the outer boundary and n_α is its normal vector that points away from the bed domain and into the fair-field. The first equality of (5.10) brings out the important fact that all variables in (5.9) are prescribed. Consequently, *the computed solution for the potential* Λ *cannot truly satisfy the field and boundary conditions* (5.6) *unless the volume rate condition* (5.9) *is satisfied.*

In formulating the second equality in (5.10), it has been assumed that the undisturbed bed is approximately plane which implies that the undisturbed bed load flux is one-dimensional and symmetrical about the streamwise axis.

I note here that, for current, Q_{bx} is constant with respect to space and therefore (5.10) yields $F = 0$. For waves based on (4.3), $F = 0$ if the crest or trough of the shear stress wave is directly above the pile axis, i.e. if $\omega t + \xi = n\pi$ where n is an integer. In all other cases, $F \neq 0$ and is computed by evaluating the right-most integral in (5.10) by quadrature.

5.4. Bed shear stress

Once the bed load flux $Q_{b\alpha}$ has been determined for the bed domain, we now face the challenge of determining the bed shear stress and the remaining model variables by either of the bed load models. In the next sub sections, I have outlined the steps for each model that involve eliminating the unknowns one by one.

Before doing so, I have two minor remarks. First, the schemes are unable to distinguish between situations with subcritical or critical Shields numbers since both situations correspond to a nil bed flux according to the bed load models. In this case, the Shields number is assumed to be critical. Secondly, the schemes for each bed load model consume about the same amount of computational resources.

5.4.1. Brørs model

To determine the model variables in the Brørs model, I have derived the following system of equations:

$$Q_{br} = Q_{b0} \cdot \left(\frac{\tau_r'}{\tau'} - c_Q \frac{\partial h}{\partial r} \right) \tag{5.11a}$$

$$Q_{b\theta} = Q_{b0} \cdot \left(\frac{\tau_\theta'}{\tau'} - \frac{c_Q}{r} \frac{\partial h}{\partial \theta} \right) \tag{5.11b}$$

$$\left(\frac{\tau_r'}{\tau'} \right)^2 + \left(\frac{\tau_\theta'}{\tau'} \right)^2 = 1 \tag{5.11c}$$

The first two equations stem from evaluating (3.7) in the polar directions through (2.3) and assuming that the Shields number is supercritical. The last equation has been derived from (2.1). The system of three equations has three unknowns, namely Q_{b0}, τ_r'/τ' and τ_θ'/τ'. The latter two can

be eliminated by rewriting the system into a single equation with the unknown Q_{b0}:

$$\left(\frac{Q_{br}}{Q_{b0}} + c_Q \frac{\partial h}{\partial r}\right)^2 + \left(\frac{Q_{b\theta}}{Q_{b0}} + \frac{c_Q}{r}\frac{\partial h}{\partial \theta}\right)^2 - 1 = 0, \quad Q_{b0} \neq 0$$

This equation that can be rewritten as a conventional quadratic equation:

$$c_{q2}\, q^2 + c_{q1}\, q + c_{q0} = 0 \tag{5.12}$$

with the following auxiliary variables:

$$q = \frac{1}{Q_{b0}}, \qquad c_{qr} = c_Q \frac{\partial h}{\partial r}, \qquad c_{q\theta} = \frac{c_Q}{r}\frac{\partial h}{\partial \theta}$$
$$c_{q2} = Q_{br}^2 + Q_{b\theta}^2, \quad c_{q1} = 2\left(Q_{br}c_{qr} + Q_{b\theta}c_{q\theta}\right), \quad c_{q0} = c_{qr}^2 + c_{q\theta}^2 - 1$$

Eq. (5.12) can then be solved analytically and the positive real root for q can be transformed back to Q_{b0}. To ensure that the solution is real or in physical terms, to avoid that the bed slope completely governs the bed load flux, the following condition must be satisfied:

$$c_Q < \frac{1}{\max\left|\dfrac{\partial h}{\partial x_\alpha}\right|} \tag{5.13}$$

In the present approach, the slope angles can be as high as the repose angle and if the latter is taken as $\phi_r = 32\,\mathrm{deg}$, the slope coefficient must be less than 1.6. This allows the use of $c_Q = 1.5$ as in Brørs (1999) but precludes the use of the upper values in the observed range $[1.5, 2.3]$ that is also stated in Brørs (1999). These considerations result in the following scheme:

1. For nodes where $Q_{br} = Q_{b\theta} = 0$, I simply take $Q_{b0} = \theta_3 = 0$ and $\zeta' = \zeta_c = \zeta_{c0}$.
2. For the remaining nodes, I do the following steps:
   (a) Prescribe c_Q.
   (b) Compute Q_{b0} by solving (5.12) analytically.
   (c) Compute τ_r'/τ' from (5.11a).
   (d) Compute angle θ_3 from $\tau_r'/\tau' = \cos\left(\theta_2 + \theta_3\right)$. This equation has been derived from Fig. 8.3 in terms of $U_{f\alpha}'$ that is co-directed with τ_α'.

(e) Compute ζ_c from (3.5).
(f) Compute ζ' by solving (3.8) for each node with the bisection method.
(g) Compute U'_f from (3.2) and (3.3).
(h) Compute C_{be} from (3.9).

5.4.2. Roulund model

To determine the model variables in the Roulund model, I do the following steps:

1. Compute $\theta_3 - \theta_4 = \mathrm{atan2}(Q_{b\theta}, Q_{br}) - \theta_2$. This equation has been derived from Fig. 8.3 in terms of $U_{b\alpha}$ that is co-directed with $Q_{b\alpha}$ according to (3.10).
2. Compute θ_5 by the equation that results from combining (3.16a) and (3.16b).
3. Compute U_{rel} by (3.16b).
4. For nodes where U_{rel} is complex-valued, update $\theta_5 := \theta_5 + \pi$ and recompute U_{rel} as in the previous step.
5. For each node:
   (a) Treat p as the unknown and solve for it by the bisection method with the initial limits $p \in]0, 1[$ and the following steps:
      i. Guess $\hat{p}$ from the actual limits.
      ii. Compute U_b from (3.10).
      iii. Compute θ_4 by the equation that results from combining (3.16c) and (3.16d).
      iv. Compute U'_f by (3.16c).
      v. If U'_f is complex-valued, update $\theta_4 := \theta_4 + \pi$ and recompute U'_f as in the previous step.
      vi. Compute θ_3 from $\theta_3 - \theta_4$ from Step 1.
      vii. Compute ζ_c by (3.5).
      viii. Compute ζ' by (3.2) and (3.3).
      ix. Compute p_* by the piece-wise formulation in (3.11).
      x. Compare p_* and $\hat{p}$ and update the limits accordingly.
      xi. Repeat Steps 5(a)i-5(a)x until convergence is acceptable.
   (b) Compute C_{be} from (3.18)–(3.19).

5.5. Entrainment rate

Once the field of the bed shear stress has been determined as described in the previous section, it is time to consider the final item of the field conditions, namely the scheme for the entrainment rate. Each guessed field of the entrainment rate e is decomposed into a predictor and corrector contribution:

$$\hat{e} = (\hat{e})_{\text{pre}} + (\hat{e})_{\text{cor}} \tag{5.14}$$

where the subscripts denote the *predictor* and *corrector* contribution, respectively. The contributions or steps are conceptually alike the predictor and corrector components of Hartvig (2011) but differ in that they are here applied to the entrainment rate and involve other steps.

The *predictor* contribution attempts to bridge the difference between the guessed and computed fields for the entrainment rate while ensuring that $\hat{e}$ approaches the undisturbed value near the outer boundary. The contribution is determined as follows:

1. Initial iteration: The predictor guess is determined from the undisturbed value at the same streamwise position, i.e. $(\hat{e})_{\text{pre}} = e|_{r_\infty}$ as given in Sec. 4.3.
2. Subsequent iterations:
   (a) Based on U_f' and C_{be} from Sec. 5.4 and Eq. (3.34), compute entrainment rate e_*.
   (b) Compute entrainment rate residual:

$$\Delta e = e_* - \hat{e} \tag{5.15}$$

   (c) Compute error measures to monitor the convergence process of the scheme:

$$\epsilon_1 = \sqrt{\frac{1}{n_{dof}} \sum_{j=1}^{n_{dof}} (\Delta e)_j^2}, \quad \epsilon_2 = \max |\Delta e|, \quad \epsilon_3 = \frac{\epsilon_2}{\max |\hat{e}|}$$

   Above, $(\Delta e)_j$ represents the entrainment rate residual at node j out of total of n_{dof} nodes and ϵ_1 to ϵ_3 are positive error measures that should decrease over-all as the entrainment rate iterations are carried out.

(d) Update predictor guess:

$$(\hat{e})_{\text{pre}} := \hat{e} + c_{\Delta e} f_{\Delta e} \Delta e \tag{5.16}$$

where $c_{\Delta e} < 1$ is a coefficient for the numerical scheme and $f_{\Delta e}$ is a ramping function. The latter satisfies $f_{\Delta e} = 1$ for $r_{\min} \leq r \leq r_d$, $f_{\Delta e} = 0$ for $r \geq r_e$ and is determined by linear interpolation with respect to the radius in the intermediate domain.

The *corrector* contribution ensures that the volume rate condition (5.9) is satisfied although, in some cases, the predictor guess may satisfy the volume rate condition approximately without the help of the corrector. The contribution is determined through the following three steps after the predictor guess has been determined:

1. Following the definition of the right equation of (5.8), compute the entrained outflux E by discrete integration of $(\hat{e})_{\text{pre}}$.
2. Compute volume rate residual R as the left-hand-side of (5.9).
3. Compute $(\hat{e})_{\text{cor}}$ as the hemiellipsoid with the origin in Origo, inner radius $r_{\min}$, outer radius r_e and the height r_{ze}. Following Hartvig (2011), the surface is taken as:

$$(\hat{e})_{\text{cor}} = \begin{cases} r_{ze} \cdot \left(1 - \left(\dfrac{r - r_{\min}}{r_e - r_{\min}}\right)^2\right)^{1/2}, & r < r_e \\ 0, & \text{else} \end{cases}$$

with the height computed as:

$$r_{ze} = \frac{6R}{\pi \cdot \left(4r_e^2 + (3\pi - 8)\, r_e r_{\min} - (3\pi - 4)\, r_{\min}^2\right)}$$

Once both contributions have been determined, the guessed entrainment rate is updated according to (5.14). The solution of e is able to converge for some configurations when the the values for $c_{\Delta e}$ are sufficiently small, the bed domain is sufficiently large and the spatial resolution is sufficiently fine.

6. Spatial Discretization & Summary

In this section, I present the spatial grid and the corresponding finite approximations. The latter are used for computing the gradient or divergence in different contexts and discretizing the potential Λ. I close the section with

a summary of the main scheme of the present model, encompassing both the boundary and field conditions.

6.1. Grid

Following Hartvig (2011), the spatial grid is shaped as a spider-web as shown in Fig. 8.5. The angle is distributed evenly as:

$$\theta_{j_\theta} = \Delta\theta \cdot (j_\theta - 1) - \pi, \quad j_\theta = 1, 2, \ldots, n_\theta \tag{6.1}$$

where $\Delta\theta = 2\pi/n_\theta$ is the angle increment and j_θ and n_θ are the actual and maximum number of nodes along the angular coordinate, respectively. To obtain the most accurate computation of quantities involving mixed derivatives, i.e. the gradient magnitude, the divergence or the Laplacian, the cells must be nearly square. Therefore, the radius is distributed as the following geometric sequence with the radius at the inner boundary of the bed domain specified as $r_{\min}$:

$$r_{j_r} = r_{\min} c_\theta^{j_r - 1}, \quad c_\theta = 1 + \Delta\theta, \quad j_r = 1, 2, \ldots, n_r \tag{6.2}$$

where j_r and n_r are the actual and maximum number of nodes in the radial direction, respectively, and the latter controls the radial extent of the outer boundary of the bed domain. The total number of nodes is $n_{dof} = n_r n_\theta$.

[Fig. 8.5 about here]

6.2. Finite differences

The first and second order derivatives of a scalar function f with respect to the *angle* are approximated by conventional central differences that follow this pattern where the subscript letters refer to the nodes in Fig. 8.5:

$$\left(\frac{\partial f}{\partial \theta}\right)_C \approx \frac{f_I - f_H}{2\Delta\theta}, \quad \text{All nodes} \tag{6.3a}$$

$$\left(\frac{\partial^2 f}{\partial \theta^2}\right)_C \approx \frac{f_I - 2f_C + f_H}{(\Delta\theta)^2}, \quad \text{All nodes} \tag{6.3b}$$

The first and second order derivatives in the *radial* direction are approximated by polar variants of *forward* differences for inner nodes, *central* differences for interior nodes and *backward* differences for outer nodes, i.e.:

$$\begin{aligned}
\left(\frac{\partial f}{\partial r}\right)_A &\approx \frac{w_1 f_C + w_2 f_B + w_3 f_A}{r_B - r_A}, && \text{Inner nodes} \\
\left(\frac{\partial f}{\partial r}\right)_C &\approx \frac{w_4 f_D + w_5 f_C + w_6 f_B}{r_D - r_B}, && \text{Interior nodes} \\
\left(\frac{\partial f}{\partial r}\right)_E &\approx \frac{w_7 f_E + w_8 f_D + w_9 f_C}{r_E - r_D}, && \text{Outer nodes}
\end{aligned} \tag{6.4a}$$

$$\left(\frac{\partial^2 f}{\partial r^2}\right)_C \approx \frac{w_{10} f_D + w_{11} f_C + w_{12} f_B}{(r_D - r_B)^2}, \quad \text{Interior nodes} \tag{6.4b}$$

where the inner, interior and outer nodes are defined in Fig. 8.5 and w_1 to w_{12} are dimensionless weights. I have determined the weights based on Taylor analysis on the radial grid (6.2) as:

$$\begin{aligned}
w_1 &= \frac{-1}{c_\theta + c_\theta^2}, & w_2 &= 1 + \frac{1}{c_\theta}, & w_3 &= \frac{-2 - c_\theta}{1 + c_\theta}, \\
w_4 &= \frac{1}{c_\theta}, & w_5 &= c_\theta - \frac{1}{c_\theta}, & w_6 &= -c_\theta, \\
w_7 &= \frac{1 + 2c_\theta}{1 + c_\theta}, & w_8 &= -1 - c_\theta, & w_9 &= \frac{c_\theta^2}{1 + c_\theta}, \\
w_{10} &= \frac{2}{c_\theta}\,(1 + c_\theta), & w_{11} &= \frac{-2}{c_\theta}\,(1 + c_\theta)^2, & w_{12} &= 2\,(1 + c_\theta)
\end{aligned}$$

The weights are also consistent with the conventional values for an even radial spacing ($c_\theta \simeq 1$). The approximations (6.3a) and (6.4a) of the first order derivatives are used to compute the divergence by (2.2) and the gradient by (2.3).

6.3. Discretization and solution of Poisson equation

The derivatives of the Poisson equation and its boundary conditions (5.6) are approximated by the corresponding finite differences (6.3b), (6.4a) and (6.4b). The system of eqs. (5.6) is then rewritten as the matrix equation:

$$A_{jm}\Lambda_j = B_m, \quad j \in 1, 2, \ldots n_{dof}, \quad m \in 1, 2. \ldots n_{dof} \tag{6.5}$$

where A_{jm} is a square $n_{dof} \times n_{dof}$ coefficient matrix that is sparsely populated, Λ_j is the vector containing the nodal values of the potential and B_m is the following load vector that represents the right-hand-sides of (5.6):

$$B_m = \begin{cases} 0, & \text{Inner nodes} \\ -C_h \dfrac{\partial h}{\partial t} - e, & \text{Interior nodes} \\ Q_{bx}|_{r_\infty} \cos\theta, & \text{Outer nodes} \end{cases} \tag{6.6}$$

The coefficient matrix A_{jm} is built once, outside the loop for the entrainment rate. When the guessed field of the entrainment rate has been computed, B_m is computed according to (6.6) and the matrix equation (6.5) is solved by a conventional row reduction method. The resulting nodal vector Λ_j is then reshaped back to a discrete scalar field Λ.

6.4. Summary of main scheme

The main scheme of the present approach can be summarized in the following steps of which steps 2–6 differ for waves or current:

1. Define input, including spatial grid, bed elevation h, bed elevation gradient $\partial h/\partial x_\alpha$, unmodified bed elevation rate $(\partial h/\partial t)_*$, scour volume rate dV/dt.
2. Prescribe undisturbed bed shear stress $\tau'_\alpha|_{r_\infty}$.
3. Compute undisturbed values:
   (a) Bed load flux $Q_{b\alpha}|_{r_\infty}$.
   (b) Entrainment rate $e|_{r_\infty}$.
   (c) Bed elevation rate $\partial h/\partial t|_{r_\infty}$.
4. Compute bed load outflux F.
5. Prescribe bed elevation rate $\partial h/\partial t$.
6. Make initial guess of entrainment rate $\hat{e}$.
7. Build coefficient matrix A_{jm} and ramping function $f_{\Delta e}$.
8. For each entrainment rate iteration:
   (a) Compute B_m and solve for the potential Λ.
   (b) Compute bed load flux $Q_{b\alpha}$.
   (c) Compute friction velocity $U'_{f\alpha}$ and C_{be}.
   (d) Update guess of entrainment rate $\hat{e}$.
   (e) Repeat steps 8a–8d until convergence is acceptable.

7. Results and discussion

In the previous sections, I presented the underlying equations and steps in the reverse approach in the context of monopile scour. In this section, I present a parametric study that exposes different aspects of the approach, compare the results with available data and infer some indications for future use.

The study is based on the experimental run A.08 of Hartvig et al. (2010) that has also been investigated in Hartvig (2011). The pile diameter is $D = 0.10\ \mathrm{m}$. The bed configuration represents a conical scour hole that has developed relatively much but not fully attained equilibrium. The scour volume is $V = 8.0\ D^3$, the scour shape factor is $\psi = 7.8$ and the scour depth is $S = (V/\psi)^{1/3} \approx D$. The far-field is subjected to the action of current or waves with the characteristic velocities $U_{cu} \approx 0.5\ \mathrm{m/s}$ or $U_m \approx 0.2\ \mathrm{m/s}$, respectively. Following the definitions in Sec. 4, this implies a live-bed state with a reference bed shear stress $\tau'_{\mathrm{ref}} = 0.5\ \mathrm{Pa}$. The reference Reynolds numbers are $R_{\mathrm{ref}} \approx 4 \cdot 10^4$ and $R_{\mathrm{ref}} \approx 2 \cdot 10^4$ during current or waves, respectively. For the wave runs, the Keulegan-Carpenter number is defined as $K \equiv U_m T/D$ and provides $K = 3$ for the present wave configuration.

Table 8.1 presents the common parameters of the configuration. Table 8.2 presents the simulations, the varying input parameters and some key results. Figs. 8.6–8.11 are pairs of contour plots of the bed surface h, the unmodified bed elevation rate $(\partial h/\partial t)_*$ and the fields of the entrainment rate, bed load flux magnitude and bed shear stress magnitude for either bed load model. In these figures, the color bar shows the minimum and maximum field values and the bold curve represent the outer boundary of the scour domain.

The simulations cover the following variations:

- The influence of bed forms in the bed surface. This has been investigated by taking the bed elevation h as h_1 or h_2 as shown in Fig. 8.6. The former is an idealized bed surface that has been created synthetically and the latter is the measured one that has been smoothened slightly. For both cases, the scour depth and scour volume are nearly identical and the slope angle is everywhere less than or equal to the repose angle since the beds have been subjected to a correction for local sliding as detailed in Hartvig (2011). For this reason, the scour hole extends slightly beyond the scour domain in h_1.

- The case of scouring or backfilling. This is denoted by S or B in the simulation name, respectively. An example of the unmodified bed

elevation rate in either case is shown in Fig. 8.7.

- The influence of the bed load model and its parameters. The identifiers Br or Ro refer to the Brørs or Roulund model, respectively. The variation of c_Q or c_u has been investigated, respectively.
- The influence of the modified bed elevation rate $(\partial h/\partial t)_{**}$ during scouring.
- The influence of the unmodified bed elevation rate $(\partial h/\partial t)_{*}$. This has been investigated in terms of the scour volume time scale t_V. For scouring, the formulation for the unmodified bed elevation rate at the pile perimeter – the *unmodified base elevation rate* b_* – has also been varied. The quantity t_V is related to the intensity of dV/dt and is central for a long-term forecasting method. The quantity b_* is related to the spatial skewness of the unmodified bed elevation rate. The parameters are detailed and illustrated in Hartvig (2011) and b_* is briefly elaborated below.

The model for the base elevation rate of Hartvig (2011) is denoted as b_{*1}. The parameter f_b is a skewness parameter where $f_b = 1$ implies no skewness of $(\partial h/\partial t)_*$ and $f_b > 1$ implies that $(\partial h/\partial t)_*$ is skewed increasingly towards the upstream domain so erosion/deposition is amplified here as illustrated in Fig. 8.7. In the present paper, I have also investigated the following formulation that can facilitate even more skewness:

$$b_{*2} = \begin{cases} b_c c_b, & |\theta| \leq \theta_{b1} \\ (|\theta| - \theta_{b2}) \dfrac{b_c - b_c c_b}{\theta_{b2} - \theta_{b1}} + b_c, & \theta_{b1} < |\theta| < \theta_{b2} \\ b_c, & \theta_{b2} \leq |\theta| \end{cases}$$

Above, b_{*2} is the alternative unmodified base elevation rate, $c_b b_c$ is the downstream value of b_{*2} before the angle θ_{b1} and b_c is the upstream value beyond the angle θ_{b2}. The upstream value b_c is computed as the dependent parameter from:

$$b_c = \frac{-2\pi \cdot (dS/dt)_{\text{pre}}}{2\pi - \theta_{b1} - \theta_{b2} + c_b\theta_{b1} + c_b\theta_{b2}}$$

where $(dS/dt)_{\text{pre}}$ is the predictor scour depth rate as detailed in Hartvig (2011) and the remaining values are given in Table 8.1.

[Tables 8.1–8.2 about here]

[Figs. 8.6–8.11 about here]

7.1. Discussion

Based on the present simulations, I make the following four comments.

First, it is clear from Table 8.2 and Figs. 8.8–8.11 that the results are particularly sensitive to the choice of the bed load model and its parameters. If we focus on the mean bed shear stress during scouring, $\tau'_{\max}/\tau'_{\text{ref}}$ varies from 1.6 to 2.6 when the bed load model or its parameters are varied. The typical spatial distribution of the bed shear stress magnitude is shown in Figs. 8.10–8.11 where the zone of the field maxima is attached to the pile at $\theta \approx 3\pi/4$. The outstanding exception is simulation S72 where the Brørs model is employed with $c_Q = 1.5$ together with the measured bed surface h_2. This simulation yields $\tau'_{\max}/\tau'_{\text{ref}} = 5.2$ detached from the pile due to a local bed variation. These trends also indicate that there can be great variation in the predicted bed elevation rate in a forward approach depending on the formulation of the bed load model.

Secondly, I have compared the computed field of the bed shear stress during scouring with the reported numerical results of Roulund et al. (2005, Sec. 6.2, Fig. 36). Using a steady Reynolds-averaged approach, they treated a configuration similar to the present one with $R_{\text{ref}} = 5 \cdot 10^4$. When the bed was plane, they obtained $\tau'_{\max}/\tau'_{\text{ref}} \approx 6$. When the scour hole was fully developed, the local scour depths were $S/D \approx 1.1$ and $S/D \approx 0.6$ in the upstream and downstream regions, respectively. In this scoured bed configuration, they obtained $\tau'_{\max}/\tau'_{\text{ref}} \approx 3$ in a zone at about $3\pi/4 \leq \theta \leq \pi$, slightly detached from the pile, presumingly due to the presence of a horseshoe vortex.

The results of Roulund et al. (2005) appear to be confirmed by the large-eddy study of Zhao and Huhe (2006, Figs. 9–10). They treated a comparable configuration with $R_{\text{ref}} = 7 \cdot 10^3$ and $S/D = 0.85$ and appear to report $\tau'_{\max}/\tau'_{\text{ref}} \approx 3$ detached in front of the pile. The laminar study of Yuhi et al. (2000, Figs. 9–10) treating a somewhat different configuration with $R_{\text{ref}} = 2 \cdot 10^3$ and $S/D = 1.2$ also confirms the same location of the maximum

bed shear stress although the maximum amplification appears to be much higher at $\tau'_{\max}/\tau'_{\text{ref}} \approx 9$, presumingly due to the horseshoe vortex being laminar.

Compared to the present results, the *location* of the zone of maximum bed shear stress differs. This discrepancy could stem from the formulation of the unmodified bed elevation rate $(\partial h/\partial t)_*$. Since this is not redeemed by varying the model for the unmodified base elevation rate b_* or its parameters, the discrepancy could stem from the more fundamental assumption in Hartvig (2011) that assumes that the strongest deposition/erosion occurs at the pile perimeter. Another plausible cause is the irrotational hypothesis in (5.5). Aside from this discrepancy, the *magnitude* of the maximum bed shear stress agrees approximately with the Brørs bed load model with $c_Q = 1.5$ that yields $\tau'_{\max}/\tau'_{\text{ref}} = 2.6$. In contrast, the Roulund model systematically underestimates the bed shear stress as $\tau'_{\max}/\tau'_{\text{ref}} \approx 2$ regardless of the variation of c_u.

Thirdly, similar model variations are observed in the case of backfilling waves although I note that the maximum magnitude $\tau'_{\max}/\tau'_{\text{ref}}$ is systematically smaller here than for current scouring. The experimental study of Sumer et al. (1997) reports $\tau'_{\max}/\tau'_{\text{ref}} \approx 3 - 4$ for a plane bed. For a scoured bed configuration around a slender monopile, the only available study to my knowledge is the numerical study of Umeda et al. (2008) for a laminar oscillatory flow. They report $\tau'_{\max}/\tau'_{\text{ref}} \approx 3$ but for a different configuration with $R_{\text{ref}} = 5 \cdot 10^3$ and $K = 20$. To obtain a more conclusive verdict of the model performance during backfilling, a detailed determination of the mean bed shear stress for a *scoured* bed configuration in waves is required.

Finally, the model results depend on the scour volume time scale t_V. The simulations indicate that a faster scouring process (e.g. S14 to S31) is related to an increase in $\tau'_{\max}/\tau'_{\text{ref}}$. Conversely, a faster backfilling process (e.g. B14 to B21) is related to a decrease in $\tau'_{\max}/\tau'_{\text{ref}}$. The simulations also indicate that the relation is quite non-linear. A ten times faster scouring process or 10 times slower backfilling process is related to only a 10-30 % increase of $\tau'_{\max}/\tau'_{\text{ref}}$. For a long-term forecasting method, these indications are encouraging and bothering at the same time. On one hand, they indicate that the time scale can be uniquely determined for a given bed shear stress field. On the other hand, even small variations in the bed shear stress change the order of magnitude of the time scale and thereby alter the forecast completely.

8. Conclusion

In conclusion, I have here presented the reverse approach and demonstrated its viability for monopile scour as seen in the contour plots in Figs. 8.6–8.10. Compared to numerical scour studies based on a forward approach, the present approach differs in the formulation of sediment pickup in (3.28) and the assumption of irrotational bed load flux (5.5). For the configuration that is considered in Sec. 7, the maximum amplification of the mean bed shear stress relative to the far-field is typically between 1.5–2.6 during scouring and 1.4–2.3 during backfilling. The maximum amplification is particularly sensitive to the bed load model and its parameters but also depends on the intensity and spatial distribution of the bed elevation rate.

Compared to the numerical studies of Roulund et al. (2005) and Zhao and Huhe (2006) for similar configurations during scouring, the present results for the mean bed shear stress appear to be in the correct order of magnitude but fail to reproduce the spatial distribution of the bed shear stress. This indicates that the model prediction is not mature yet and could perhaps be improved by changing the formulation of the underlying unmodified bed elevation rate of Hartvig (2011). For backfilling, no comparable studies appear to be available.

To facilitate a more conclusive assessment and provide data for calibration, future detailed studies are encouraged. These should treat the near-bed flow – including the distribution of the mean bed shear stress – around a monopile in a *scoured* bed configuration subjected to current or waves.

Acknowledgment

This study is a part of my PhD study which has been partially funded by Dong Energy Ltd.

References

R. A. Bagnold. Experiments on a gravity-free dispersion of large solid spheres in a newtonian fluid under shear. In *Proc. Royal Society of London. Series A, Mathematical and Physical Sciences*, volume 225, pages 49–53. Royal Society, 1954.

B. Brørs. Numerical modeling of flow and scour at pipelines. *J. Hydraulic Eng.*, 125(5):511–523, 1999. ISSN 0022-1120. doi: 10.1061/(ASCE)0733-9429(1999)125:5(511).

Subhasish Dey and Abdul Karim Barbhuiya. Time variation of scour at abutments. *J. Hydraulic Eng.*, 131(1):11–23, 2005. doi: 10.1061/(ASCE)0733-9429(2005)131:1(11).

Subhasish Dey and Koustuv Debnath. Sediment pickup on streamwise sloping beds. *J. Irrigation and Drainage Eng.*, 127(1):39–43, 2001. doi: 10.1061/(ASCE)0733-9437(2001)127:1(39).

Frank Engelund and Jørgen Fredsøe. A sediment transport model for straight alluvial channels. *Nordic Hydrology*, 7(5):293–306, 1976.

Jørgen Fredsøe and Rolf Deigaard. *Mechanics of coastal sediment transport*, volume 3 of *Advances series on Ocean Eng.* World Scientific, 1992. ISBN 981-02-0840-5.

Marcelo Garcia and Gary Parker. Entrainment of bed sediment into suspension. *J. Hydraulic Eng.*, 117(4):414–435, 1991. doi: 10.1061/(ASCE)0733-9429(1991)117:4(414).

Peres Akrawi Hartvig. Model for the evolving bed surface around an offshore monopile. 2011. In review.

Peres Akrawi Hartvig, Jess McCann Thomsen, Peter Frigaard, and Thomas Lykke Andersen. Experimental study of the development of scour & backfilling. *Coastal Eng. J.*, 52(2):157–194, 2010. ISSN 0578-5634. doi: 10.1142/S0578563410002154.

Peter Nielsen. *Coastal bottom boundary layers and sediment transport*, volume 4 of *Advances series on Ocean Eng.* World Scientific, 1992. ISBN 981-02-0472-8.

Leo C. van Rijn. Sediment transport, part ii: Suspended load transport. *J. Hydraulic Eng.*, 110(11):1613–1641, 1984b. ISSN 0733-9429/84/0011-1613. doi: 10.1061/(ASCE)0733-9429(1984)110:11(1613). URL http://www.leovanrijn-sediment.com.

Leo C. van Rijn. Sediment pick-up functions. *J. Hydraulic Eng.*, 110 (10):1494–1502, 1984d. doi: 10.1061/(ASCE)0733-9429(1984)110:10(1494). URL http://www.leovanrijn-sediment.com.

Leo C. van Rijn. Mathematical models for sediment concentration profiles in steady flow. In *Transport of Suspended Solids in Open Channels: Proc. Euromech 192, Munich, Neubiberg, Germany*, 1985. URL http://www.leovanrijn-sediment.com.

Andreas Roulund, B. Mutlu Sumer, Jørgen Fredsøe, and Jess Michelsen. Numerical and experimental investigation of flow and scour around a circular pile. *J. Fluid Mechanics*, 534:351–401, 2005. ISSN 0022-1120. doi: 10.1017/S0022112005004507.

B. M. Sumer, N. Christiansen, and J. Fredsøe. The horseshoe vortex and vortex shedding around a vertical wall-mounted cylinder exposed to waves. *J. Fluid Mechanics*, 332:41–70, 1997.

Shinya Umeda, Masatoshi Yuhi, and Hajime Ishida. Three-dimensional numerical model for wave-induced scour around a vertical cylinder. In Jane McKee Smith, editor, *Proc. 31st Int. Conf. of Coastal Eng., Hamburg*, pages 2717–2729. World Scientific, 2008. doi: 10.1142/9789814277426_0224.

A. Melih Yanmaz. Temporal variation of clear water scour at cylindrical bridge piers. *Canadian J. Civil Eng.*, 33(8):1098 – 1102, 2006. ISSN 03151468.

M. Yuhi, H. Ishida, and S. Umeda. A numerical study of three-dimensional flow fields around a vertical cylinder mounted on a bed. In I. J. Losada, editor, *Proc. International Conf. Coastal Structures '99*, pages 783–792. Balkema Publishers, 2000. ISBN 90-5809-092-2.

Wei Zhao and Aode Huhe. Large-eddy simulation of three-dimensional turbulent flow around a circular pier. *J. Hydrodynamics*, 18(6):765–772, 2006. doi: 10.1016/S1001-6058(07)60019-5.

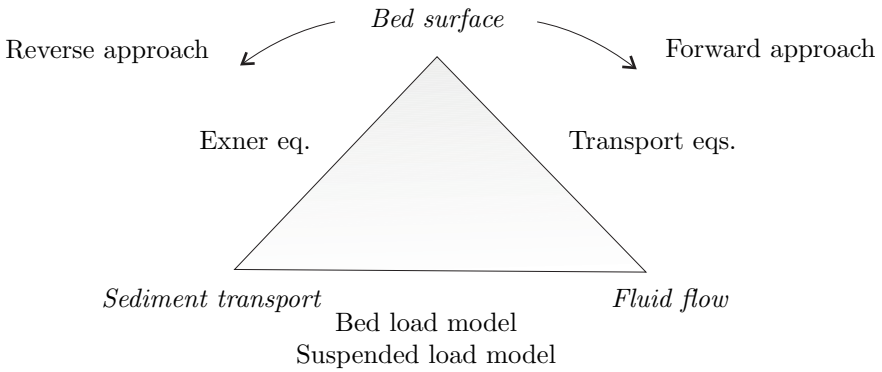

Figure 8.1: Interaction between the bed surface, the fluid flow and the sediment transport. The present paper demonstrates the reverse approach

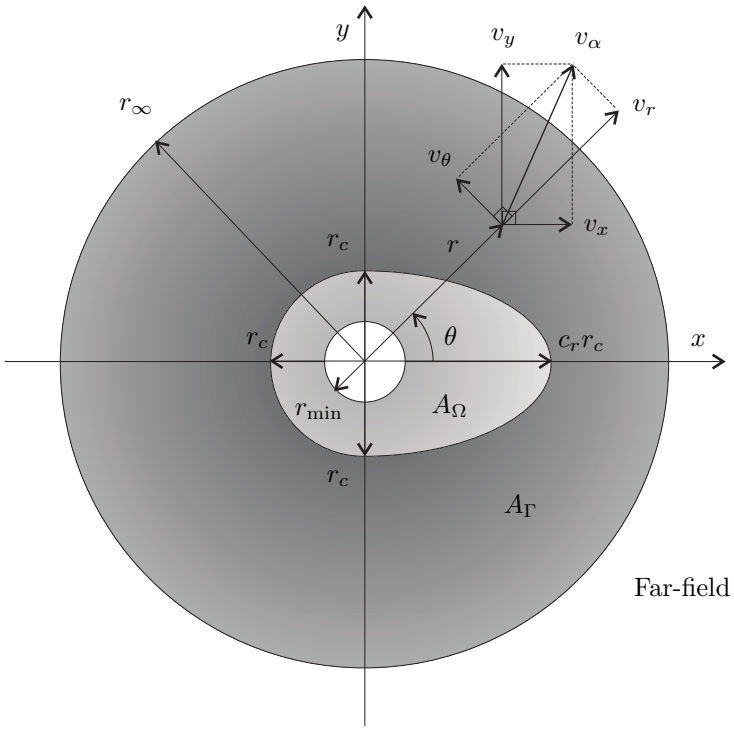

Figure 8.2: Definition of domain. The dimensions of the pile and the scour domain have been magnified

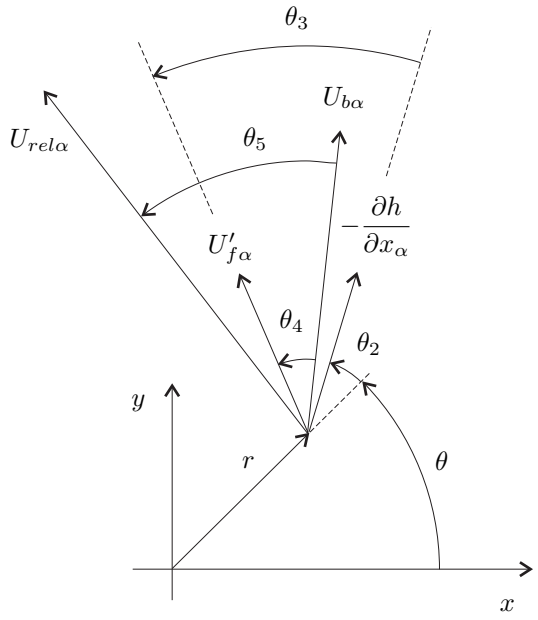

Figure 8.3: Definition of angles

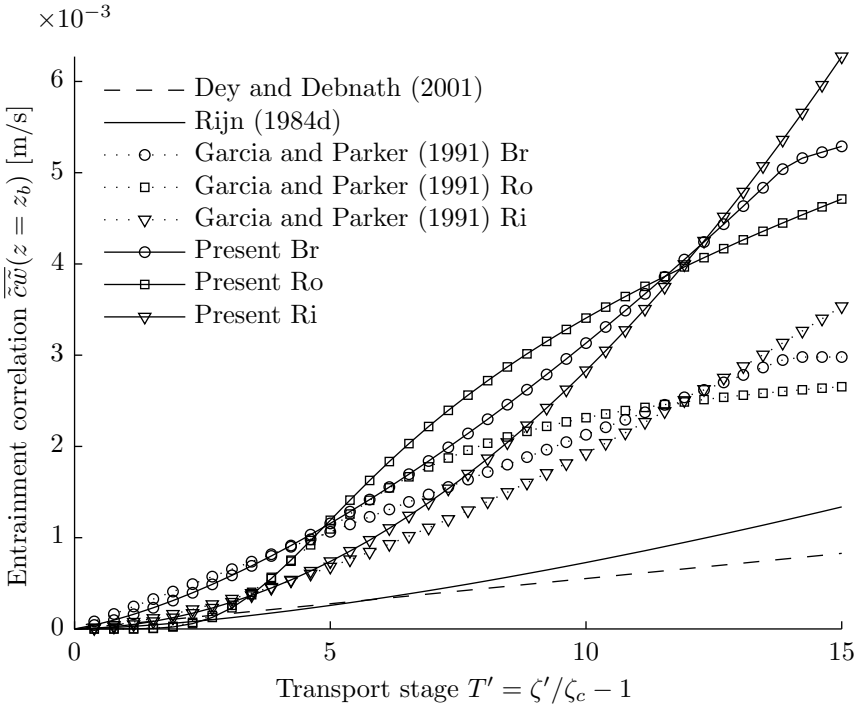

Figure 8.4: Entrainment correlation as function of transport stage according to different models

Table 8.1: Common properties. Estimated values are denoted with †. For simulation S33, the values $n_\theta = 500$, $n_r = 384$ and $r_\infty \approx 60D$ are adopted

Group	Property	Value
Sediment	Characteristic grain diameter	$d = 0.15$ mm
	Grain concentration maximum	$C_{\max} = 0.65$ †
	Grain concentration in bed	$C_h = 0.6$ †
	Static friction coefficient	$\mu_s = 0.62$
	Dynamic friction coefficient	$\mu_d = 0.51$ †
Fluid	Fluid density	$\rho_f = 1000\,\mathrm{kg/m^3}$ †
	Fluid viscosity	$\nu = 1.3 \cdot 10^{-6}\,\mathrm{m^2/s}$ †
Sediment-fluid	Gravity acceleration	$g = 9.81\,\mathrm{N/kg}$ †
	Relative grain-fluid density	$s = 2.65$ †
	Critical Shields number for plane bed	$\zeta_{c0} = 0.05$
	Sediment-fluid coefficient	$c_l = 0.027$ †
	Settling speed, computed from (3.32)	$W_{d0} = 0.01\,\mathrm{m/s}$
Bed domain	Pile radius	$r_{\min} = 0.05\,\mathrm{m} = D/2$
	Scour domain parameters	$r_c = 0.23\,\mathrm{m}$, $c_r = 1.2$
	Ramp inner and outer radii	$r_d = 0.2\,r_\infty$, $r_e = 0.3\,r_\infty$
	Outer boundary radius	$r_\infty \approx 20\,D$
Numerical resolution	Angular resolution	$n_\theta = 400$
	Radial resolution	$n_r = 238$
	Entrainment rate iteration coefficient	$0.01 \leq c_{\Delta e} \leq 0.10$
Unmodified bed elevation rate	Common properties	$V_0 = 8.0\,D^3$, $\psi_0 = 7.8$
	Current properties	$\psi_\infty = 7.5$, $t_\psi = 1\mathrm{min}$, $r_h = r_c$
	Wave properties	$c_1 = 250$, $c_2 = 1.9$
	b_{*1} properties	$c_p = 1$
	b_{*2} properties	$c_b = 0$, $\theta_{b1} = \pi$, $\theta_{b2} = 3\pi/4$
Load conditions	Reference bed shear stress	$\tau'_{\mathrm{ref}} = 0.5$ Pa
	Reference friction velocity	$U'_{f\mathrm{ref}} = 0.0224\,\mathrm{m/s}$
	Time	$t = 0$
	Wave properties	$L = 2.6\,\mathrm{m}$, $\xi = 0$, $T = 1.64\,\mathrm{s}$

Table 8.2: Simulations and varying parameters. The simulations in bold are illustrated in Figs. 8.8–8.11

Name	Bed load model		Bed	Unmodified bed elevation rate					Volume rates				Field maxima		
	Br/Ro	c_Q, c_u	h	b_*	f_b	t_V	V_∞/D^3	U'_{fe}	dV/dt	M	F	E	$e_{\max}$	$\tau'_{\max}/\tau'_{\text{ref}}$	$Q_{b\,\max}/Q_{b\text{ref}}$
		–			-	min	–	m/s	m^3/s	m^3/s	m^3/s	m^3/s	m/s	–	–
S11	Br	0	h_1	b_{*1}	1.05	9.5	13.7	0.0224	$1.0 \cdot 10^{-5}$	0	0	$6.0 \cdot 10^{-6}$	$3.1 \cdot 10^{-4}$	1.6	2.4
S12	Br	0.5	h_1	b_{*1}	1.05	9.5	13.7	0.0224	$1.0 \cdot 10^{-5}$	0	0	$6.0 \cdot 10^{-6}$	$4.2 \cdot 10^{-4}$	1.7	2.6
S13	Br	1.0	h_1	b_{*1}	1.05	9.5	13.7	0.0224	$1.0 \cdot 10^{-5}$	0	0	$6.0 \cdot 10^{-6}$	$6.0 \cdot 10^{-4}$	1.9	2.7
S14	**Br**	**1.5**	$\boldsymbol{h_1}$	$\boldsymbol{b_{*1}}$	**1.05**	**9.5**	**13.7**	**0.0224**	$\mathbf{1.0 \cdot 10^{-5}}$	**0**	**0**	$\mathbf{6.0 \cdot 10^{-6}}$	$\mathbf{1.3 \cdot 10^{-3}}$	**2.6**	**2.6**
S21	Br	1.5	h_1	b_{*1}	4/3	9.5	13.7	0.0224	$1.0 \cdot 10^{-5}$	0	0	$6.0 \cdot 10^{-6}$	$1.4 \cdot 10^{-3}$	2.7	2.7
S22	Br	1.5	h_1	b_{*2}	–	9.5	13.7	0.0224	$1.0 \cdot 10^{-5}$	0	0	$6.0 \cdot 10^{-6}$	$1.5 \cdot 10^{-3}$	2.8	3.0
S31	Br	1.5	h_1	b_{*1}	1.05	0.95	13.7	0.0224	$1.0 \cdot 10^{-4}$	0	0	$6.0 \cdot 10^{-5}$	$2.2 \cdot 10^{-3}$	3.3	3.9
S32	Br	1.5	h_1	b_{*1}	1.05	95	13.7	0.0224	$1.0 \cdot 10^{-6}$	0	0	$6.0 \cdot 10^{-7}$	$1.2 \cdot 10^{-3}$	2.5	2.5
S33	Br	1.5	h_1	b_{*1}	1.05	9.5	13.7	0.0224	$1.0 \cdot 10^{-5}$	$5.0 \cdot 10^{-6}$	0	$3.0 \cdot 10^{-6}$	$6.0 \cdot 10^{-4}$	1.8	2.6
S41	**Ro**	**10**	$\boldsymbol{h_1}$	$\boldsymbol{b_{*1}}$	**1.05**	**9.5**	**13.7**	**0.0224**	$\mathbf{1.0 \cdot 10^{-5}}$	**0**	**0**	$\mathbf{6.0 \cdot 10^{-6}}$	$\mathbf{5.2 \cdot 10^{-4}}$	**1.7**	**2.5**
S42	Ro	100	h_1	b_{*1}	1.05	9.5	13.7	0.0224	$1.0 \cdot 10^{-5}$	0	0	$6.0 \cdot 10^{-6}$	$2.7 \cdot 10^{-4}$	1.5	2.1
S43	Ro	5	h_1	b_{*1}	1.05	9.5	13.7	0.0224	$1.0 \cdot 10^{-5}$	0	0	$6.0 \cdot 10^{-6}$	$4.3 \cdot 10^{-4}$	1.6	2.3
S51	Ro	10	h_1	b_{*1}	4/3	9.5	13.7	0.0224	$1.0 \cdot 10^{-5}$	0	0	$6.0 \cdot 10^{-6}$	$6.3 \cdot 10^{-4}$	1.8	2.6
S52	Ro	10	h_1	b_{*2}	–	9.5	13.7	0.0224	$1.0 \cdot 10^{-5}$	0	0	$6.0 \cdot 10^{-6}$	$7.6 \cdot 10^{-4}$	2.0	2.8
S61	Ro	10	h_1	b_{*1}	1.05	0.95	13.7	0.0224	$1.0 \cdot 10^{-4}$	0	0	$6.0 \cdot 10^{-5}$	$1.1 \cdot 10^{-3}$	2.2	3.1
S62	Ro	10	h_1	b_{*1}	1.05	95.0	13.7	0.0224	$1.0 \cdot 10^{-6}$	0	0	$6.0 \cdot 10^{-7}$	$4.2 \cdot 10^{-4}$	1.6	2.3
S71	Br	1.0	h_2	b_{*1}	1.05	9.5	13.7	0.0224	$1.0 \cdot 10^{-5}$	0	0	$6.0 \cdot 10^{-6}$	$7.5 \cdot 10^{-4}$	2.1	2.8
S72	Br	1.5	h_2	b_{*1}	1.05	9.5	13.7	0.0224	$1.0 \cdot 10^{-5}$	0	0	$6.0 \cdot 10^{-6}$	$37 \cdot 10^{-3}$	5.2	3.1
S73	Ro	10	h_2	b_{*1}	1.05	9.5	13.7	0.0224	$1.0 \cdot 10^{-5}$	0	0	$6.0 \cdot 10^{-6}$	$6.6 \cdot 10^{-4}$	1.9	2.6
B11	Br	0	h_1	b_{*1}	1.0	113	0.1	0.0204	$-1.2 \cdot 10^{-6}$	$-1.5 \cdot 10^{-5}$	0	$8.4 \cdot 10^{-6}$	$3.2 \cdot 10^{-4}$	1.4	2.0
B12	Br	0.5	h_1	b_{*1}	1.0	113	0.1	0.0204	$-1.2 \cdot 10^{-6}$	$-1.5 \cdot 10^{-5}$	0	$8.4 \cdot 10^{-6}$	$4.4 \cdot 10^{-4}$	1.5	2.2
B13	Br	1.0	h_1	b_{*1}	1.0	113	0.1	0.0204	$-1.2 \cdot 10^{-6}$	$-1.5 \cdot 10^{-5}$	0	$8.4 \cdot 10^{-6}$	$6.4 \cdot 10^{-4}$	1.8	2.3
B14	Br	1.5	h_1	b_{*1}	1.0	113	0.1	0.0204	$-1.2 \cdot 10^{-6}$	$-1.5 \cdot 10^{-5}$	0	$8.4 \cdot 10^{-6}$	$1.3 \cdot 10^{-3}$	2.4	2.3
B21	Br	1.5	h_1	b_{*1}	1.0	11.3	0.1	0.0204	$-1.2 \cdot 10^{-5}$	$-1.5 \cdot 10^{-5}$	0	$2.1 \cdot 10^{-6}$	$1.0 \cdot 10^{-3}$	2.2	2.0
B22	Br	1.5	h_1	b_{*1}	1.0	1130	0.1	0.0204	$-1.2 \cdot 10^{-7}$	$-1.6 \cdot 10^{-5}$	0	$9.3 \cdot 10^{-6}$	$1.3 \cdot 10^{-3}$	2.4	2.3
B31	Ro	10	h_1	b_{*1}	1.0	113	0.1	0.0216	$-1.2 \cdot 10^{-6}$	$-1.3 \cdot 10^{-6}$	0	$9.1 \cdot 10^{-8}$	$3.8 \cdot 10^{-4}$	1.5	2.2
B32	Ro	10	h_1	b_{*1}	1.0	11.3	0.1	0.0216	$-1.2 \cdot 10^{-5}$	$-1.3 \cdot 10^{-6}$	0	$-6.2 \cdot 10^{-6}$	$3.0 \cdot 10^{-4}$	1.4	2.0
B33	Ro	10	h_1	b_{*1}	1.0	1130	0.1	0.0216	$-1.2 \cdot 10^{-7}$	$-1.3 \cdot 10^{-6}$	0	$7.2 \cdot 10^{-7}$	$3.8 \cdot 10^{-4}$	1.5	2.2

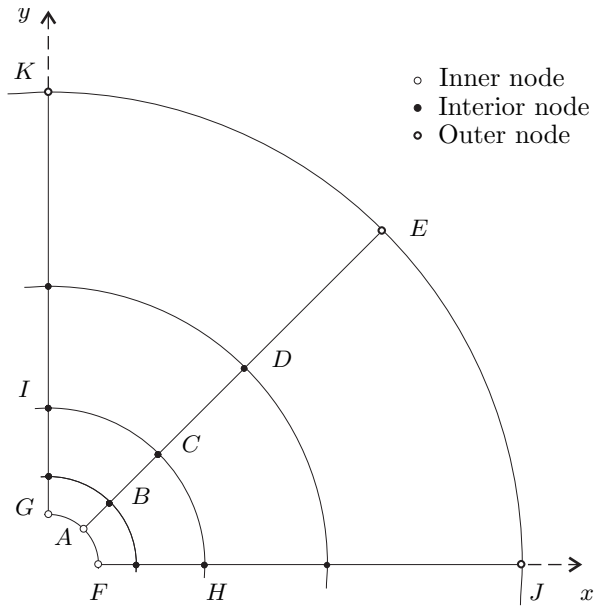

Figure 8.5: Example of spatial grid with $n_\theta = 8$ and $n_r = 5$. The entire grid is not shown

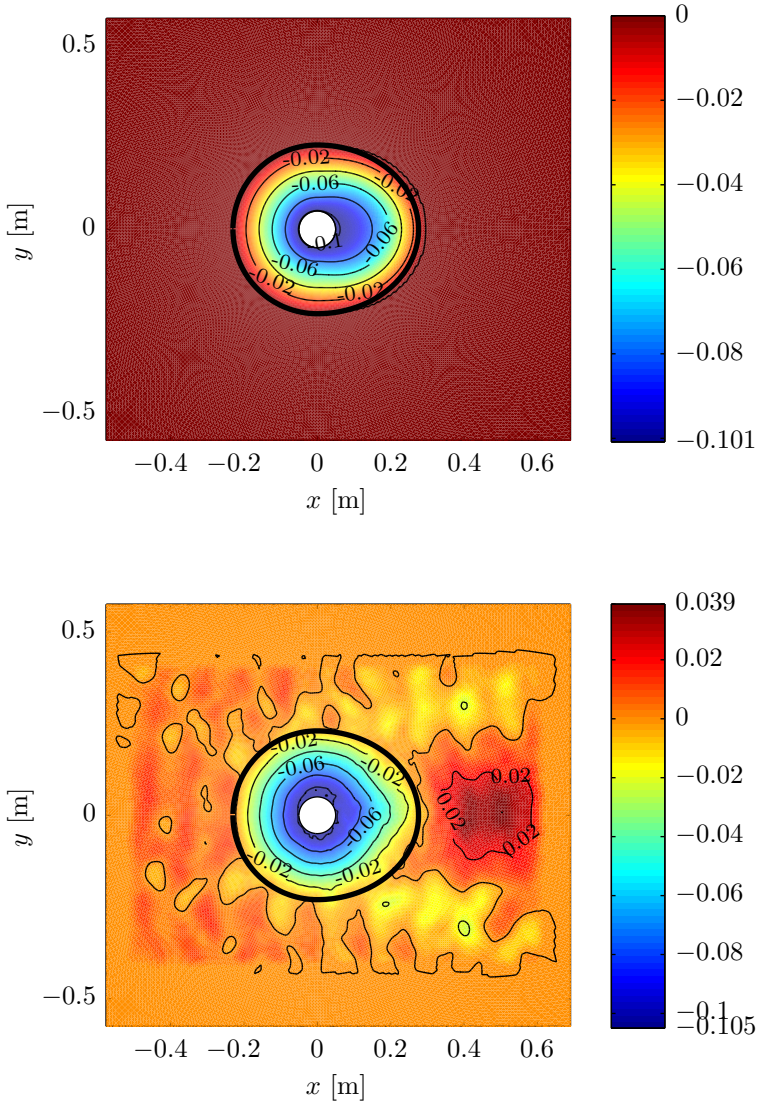

Figure 8.6: Bed elevation h [m]. Above a: Idealized h_1. Below b: Measured h_2

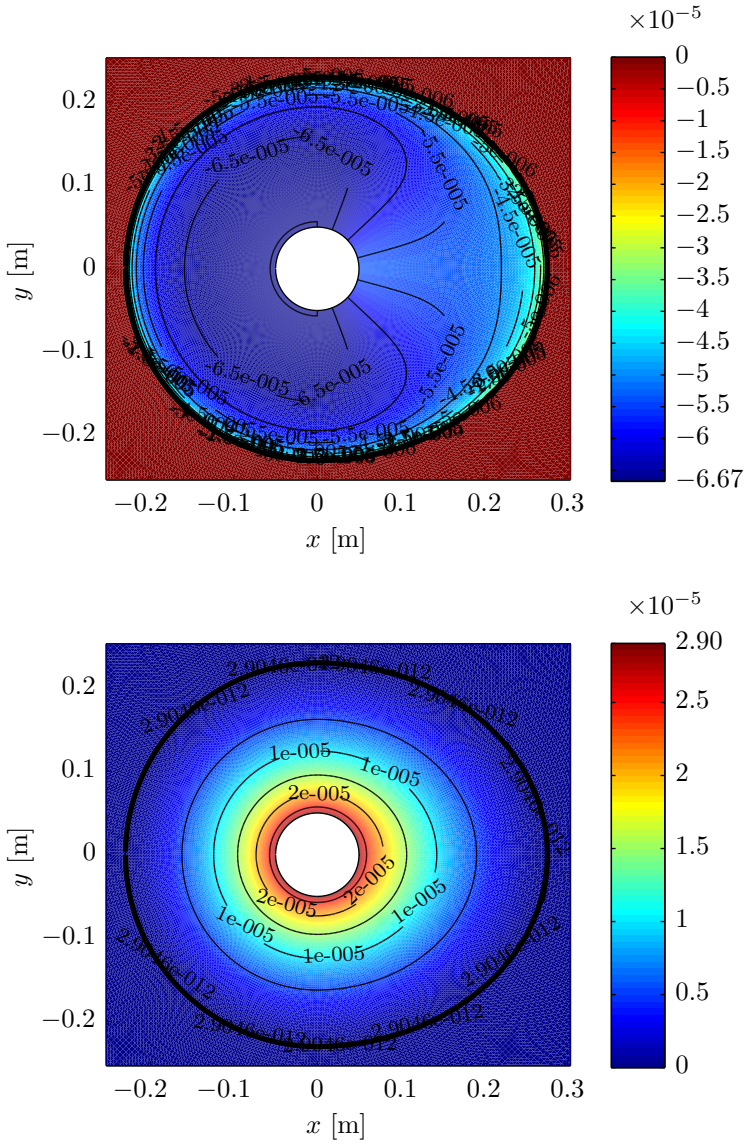

Figure 8.7: Unmodified bed elevation rate $(\partial h/\partial t)_*$ [m/s]. Above a: $f_b = 1.05$, $t_V = 9.5$ min. Below b: $f_b = 1.0$, $t_V = 113$ min

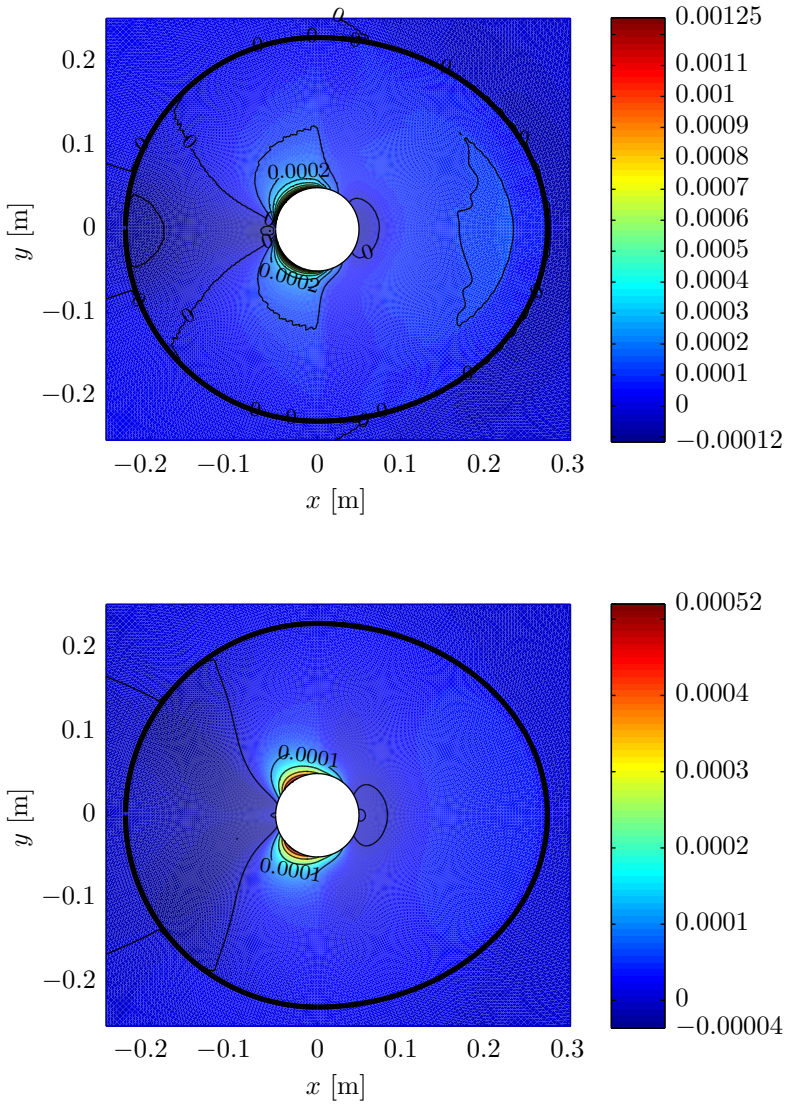

Figure 8.8: Entrainment rate e [m/s]. Above a: S14. Below b: S41

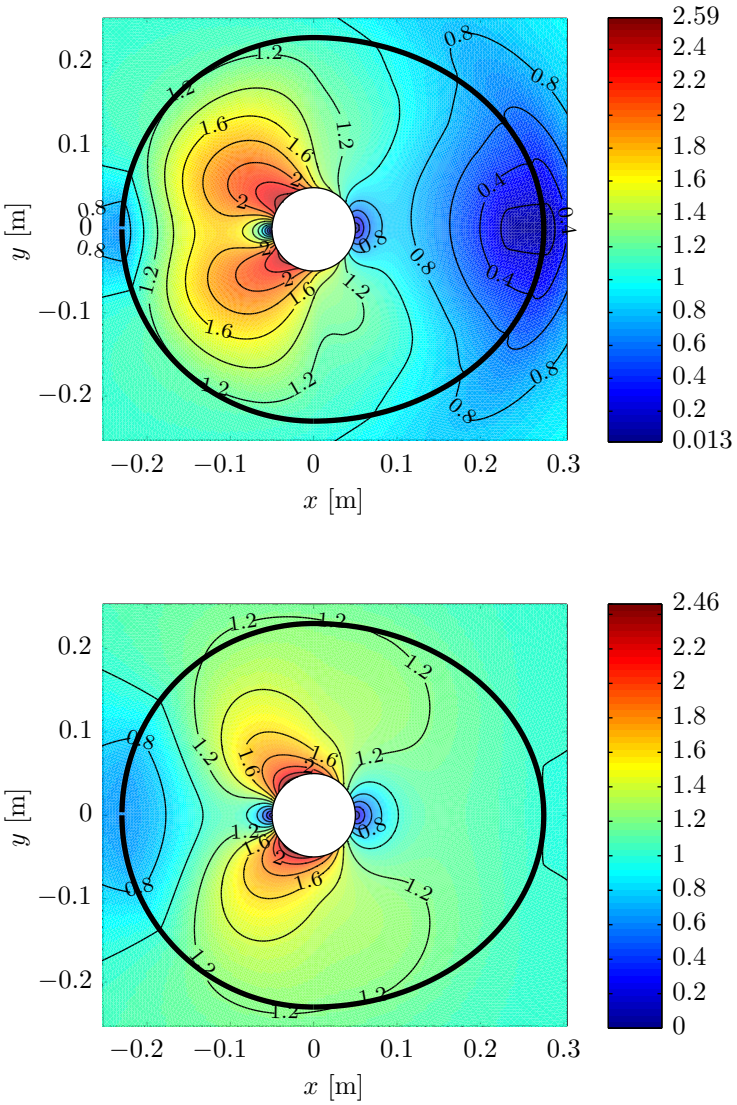

Figure 8.9: Bed load flux amplification Q_b/Q_{bref}. Above a: S14. Below b: S41

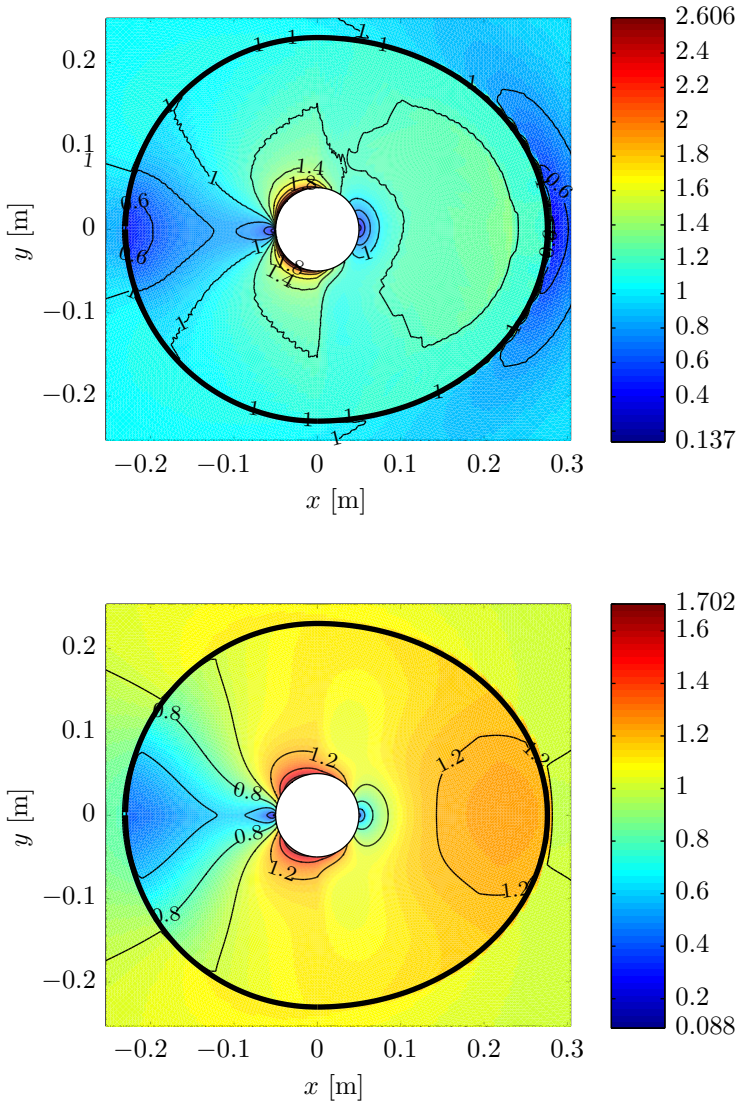

Figure 8.10: Bed shear stress amplification τ'/τ'_{ref}. Above a: S14. Below b: S41

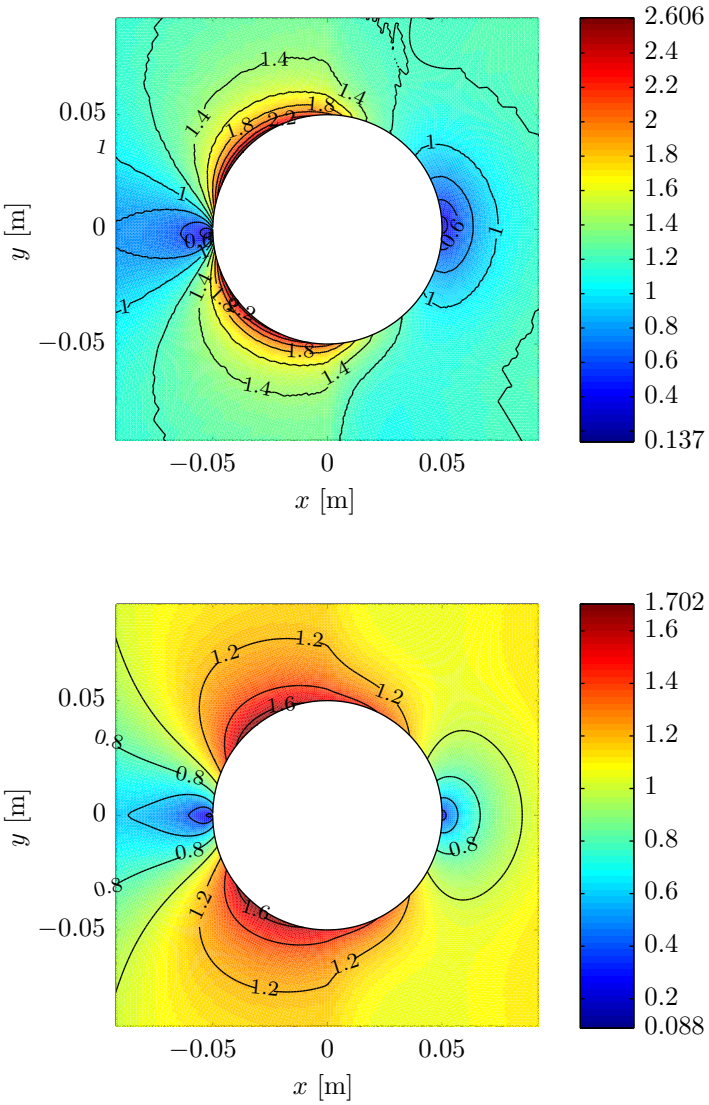

Figure 8.11: Bed shear stress amplification τ'/τ'_{ref}. Above a: S14. Below b: S41